TFTR MIRNOV COIL ANALYSIS AT PLASMA START-UP

Thomas R. Harley, Dean A. Buchenauer, John Coonrod, Kevin M. McGuire

Plasma Physics Laboratory,
Princeton University,
Princeton, New Jersey 08544

PPPL--2298
DE86 006354

ABSTRACT. The methods for finding poloidal and toroidal numbers of MHD oscillations from Mirnov coils are reviewed and modified. Examples of various MHD phenomena occurring during start-up on TFTR are illustrated. It is found that the MHD mode structure best fits a model with the toroidal correction [1,2] included.

A new algorithm which finds m, n numbers can accommodate toroidal effects which are manifested in the phase data. The algorithm can find m, n numbers with a given toroidal correction parameter λ', ($\lambda' = 0 \Rightarrow$ cylindrical). This algorithm is also used to find the optimal value of λ' automatically, eliminating the need for "guesswork." The algorithm finds the best parameters to the fit much faster than more conventional computational techniques.

I. INTRODUCTION

Evidence of magnetic islands in a tokamak plasma is given by the external magnetic field fluctuations which Mirnov coils detect. Correlating the phases from an array of Mirnov coils yields useful information about the geometry of a mode's magnetic perturbations. In Sec. II of this paper, the techniques involved in analyzing data from an array of Mirnov coils are reviewed and modified. This data analysis takes into account the increased spatial variation of the mode on the inner side of the tokamak. The analysis techniques are especially helpful for analyzing modes in the plasma with $m \geq 4$.

Section III contains results obtained by using these analysis techniques on TFTR start-up data. Particular emphasis is given to measuring the degree of poloidal asymmetry in the magnetic perturbations. These results are compared with theoretical predictions for the first order toroidal correction. Effects due to the displacement of the mode's center away from the vacuum vessel center are also investigated. The combined effect due to toroidicity and the off-center position provides a strong motivation for using a free toroidal correction parameter when fitting the phase data from the Mirnov coils.

An algorithm was developed to minimize the computational time and length of code necessary to calculate the m, n numbers for a given set of phase data. This algorithm is particularly useful for anyone analyzing Mirnov coil data in order to find m, n numbers. Analytical solutions for the parameters in the phase fit may be found for all the parameters used in the fit to the Mirnov phase data.

II. METHOD

The locations of the Mirnov coils in TFTR are given in Fig. 1. The coils are located 110 cm from the vacuum vessel center and are oriented in order to detect $\dot{B}_\theta$. The poloidal array formed by coils 1–16 detect the m number and coils 17–19 are used to determine the n number. Techniques for analyzing data from these signals are well known.[3] First a Mirnov signal, depicted in Fig. 2(a), is inspected for regions of high MHD activity. After expanding the region of interest, the $\dot{B}_\theta$ signal usually appears sinusoidal when a clear mode is present. If the signal is large enough, one can often determine the m number of the mode as the number of maxima that pass by at a fixed time on an overlaid plot of the Mirnov signals from the poloidal array, as Fig. 2(b) illustrates. This method is less misleading if the signal from the first coil (plotted at the bottom) is plotted again at the top [unlike the diagram in Fig. 2(b)] to more easily see that the signal on channel 1 is "lagging" far behind channel 16 rather than "leading" it slightly, so that 6 "ridges" can be observed to cross any vertical line.

One should choose a time range which is large enough for a fast Fourier transform to single out relevant oscillation frequencies in the signal above the background noise. The time range should be small enough, however, so that the mode's frequency does not vary too much over the time range to be fast Fourier transformed, and so that regions where too much noise is on the signals may be avoided. Time ranges for which a mode was present and the data were suitable for phase correlation analysis were most efficiently found by observing Mirnov signals from the poloidal array on overlaid plots.

Analysis of the data shown in Fig. 2(b) is given in Fig. 3. Although the average of all the Mirnov coil's amplitudes at a given frequency for a wide range of frequencies [Fig. 3(a)] has little quantitative meaning, it is useful to determine the frequency of the mode which the Mirnov coils detect. The corresponding data from a single Mirnov coil may contain misleading peaks due to noise on that signal.

Having chosen the frequency of interest, the phase angles from each Mirnov coil taken at that frequency are investigated [as in Fig. 3(b)]. At this point one may attempt to find the best cylindrical fit [Fig. 3(c)] to the phases. This involves finding the optimal m, n, δ_0 parameters such that $\xi = m\theta + n\phi + \delta_0$ approximates the phase data. Here δ_0 is a phase constant and θ, ϕ are the poloidal and toroidal angles of the Mirnov coils. A more reliable method for finding m, n numbers (especially for $m \geq 4$) is finding the optimal fit with four free parameters, *i.e.*, $\xi = m(\theta + \lambda' \sin\theta) + n\phi + \delta_0$. The added free (toroidal correction) parameter, λ', enables the fit to allow for toroidal corrections to the geometry of the mode and the off-center position of the mode with respect to the center of the vacuum vessel. Figure 3(d) illustrates the optimal toroidal fit.

Figure 4 illustrates typical failure of the cylindrical approximation to determine m, n numbers correctly. The optimal cylindrical fit is depicted by the dashed line which indicates $m = 3$. The solid line indicates the contrasting optimal toroidal fit which determined $m = 4$ correctly. This solid line fit was found by leaving λ' as a free parameter. The number of times the fit wraps around the top of the graph indicates the m number of the fit.

Since λ' is found by the computer, the difficulty of having to estimate λ' for the flux surface on which the mode lies is removed. This automation is especially useful for analyzing start-up data ($m \geq 4$) to obtain m, n numbers as well as gain useful information about the geometry of the tearing mode.

Another method is available for obtaining a more concrete idea of what the geometry of the mode's poloidal field variations looks like.[4] Let $a(i)$ and $ph(i)$ be the amplitude and phase angle for each Mirnov coil taken at the frequency of interest. Let $\theta(i)$ represent the poloidal angle of the i^{th} Mirnov coil. Define $\hat{r}(\theta)$ as the cubic spline fit which interpolates the data points, $\{\theta(i), r(i) = a(i)\cos[ph(i)] + C\}_{i=1}^{N}$. A polar plot of the $\hat{r}(\theta)$ fit then indicates the m number, according to the number of "humps" that are present. These polar plots can be thought of as a "snapshot" of the mode's poloidal magnetic field variations. Emphasizing only one Fourier component from the signals merely attempts to filter out noise from sources other than the mode.

This method breaks down for large values of m. As the difference between the phases from adjacent Mirnov coils (1–16) increases, it becomes more probable that one of the "humps" will be missed. Figure 5 illustrates four different methods of analyzing the same data. In Fig. 5(a) the optimal cylindrical fit indicates $m = 4$, and in Fig. 5(b) the polar plot indicates $m = 5$. The optimal toroidal fit shown in Fig. 5(c) correctly determined that $m = 6$. A careful examination of a corrected $m = 6$ polar plot in Fig. 5(d) reveals that a "hump" between the 16^{th} and 1^{st} Mirnov coils was missed in Fig. 5(b). Figure 5(b) demonstrates that the m number resolution obtained from directly interpolating the $\{\theta(i), r(i)\}_{i=1}^{N}$ data was unreliable for $m > 5$. The technique that was used to produce the corrected polar plot in Fig. 5(d) was accurate for much higher m numbers.

The technique employed to construct this corrected $m = 6$ polar plot is illustrated in Fig. 6. The (optimal toroidal) phase fit is depicted by the curved solid line in Fig. 6(a). The differences between the Mirnov coil phases and this phase fit are evaluated at each Mirnov coil position and plotted against poloidal angle in Fig. 6(b). This is interpolated by a cubic spline, which is also given in Fig. 6(b). This spline is added to the phase fit in order to obtain a corrected phase fit which actually interpolates the phase data. The cubic spline fit in Fig. 6(c) interpolates the amplitude data of the Mirnov coils (versus poloidal angle). Now the $\{\theta(i), r(i) = a(i)\cos[\theta(i)] + C\}_{i=1}^{N}$ data are interpolated with the product of the amplitude spline times the cosine of the corrected phase fit (plus a constant) in Fig. 6(d). To reiterate this more symbolically, let the interpolating cubic spline (ics) of $\{x_i, y_i\}_{i=1}^{N}$ be denoted by $y(x) = ics(x) = ics[\{x_i, y_i\}_{i=1}^{N}, x]$. The fit, $\xi(\theta) = m(\theta + \lambda' \sin\theta) + n\phi + \delta_0$, is adjusted to $\hat{\xi}(\theta) = \xi(\theta) + ics[\{\theta(i), ph(i) - \xi[\theta(i)]\}_{i=1}^{N}, \theta]$ so that $\hat{\xi}[\theta(i)] = ph(i)$. Letting $\hat{a}(\theta) = ics[\{\theta(i), a(i)\}_{i=1}^{N}, \theta]$, the corrected polar plot is then constructed from $\hat{r}(\theta) = \hat{a}(\theta)\cos[\hat{\xi}(\theta)] + C$. This technique gives a much better picture of the mode's geometry as Fig. 6(d) illustrates. Using the interpolation of the phase data, $ph(i)$, instead of only utilizing the cosine of the phase data by directly interpolating $r(i) = a(i)\cos[ph(i)] + C$, avoids losing useful information about the phases, for example, $\cos(-15^\circ) = \cos(15^\circ)$.

The polar plot in Fig. 6(e) depicts the same data and interpolation as Fig. 6(d), plotted against $\theta^* = \theta + \lambda' \sin\theta$ instead of θ. This should transform the mode into a cylindrical geometry, according to the degree that $\xi = m\theta^* - n\phi + \delta_0$ is an appropriate model for the phase data.

All of the polar plots given in the remainder of this paper show $\hat{r}(\theta)$ plotted against θ as obtained by the described method for constructing corrected polar plots.

III. PHYSICS

With the exception of Fig. 19 all of the data shown in this report was taken from shot #9689 (6/22/84) during start-up. This was a typical discharge for TFTR. The current flat topped at 1 MA at $t = 1$ sec. This was an ohmic heating discharge with $B_T = 2.8$ T.

A. Parameters

Figures 7–8 give the relevant parameters of the shot for the 0 to 0.6 sec time range for which analysis from the Mirnov coils will be given. $\Lambda = \beta_\theta + l_i/2$ (where l_i is the internal inductance per unit length), the major radius of the plasma, the plasma current, and the Shafranov q value at the edge of the plasma are shown in Fig. 7. Figure 8 gives the line-averaged density.

B. Evolution of detected modes

Figure 9 gives the Mirnov signal on coil #9 (see Fig. 1). The modes which were detected and the time range for which they could be found is shown above the signal. A correlation between increased MHD activity and the time ranges when a mode is present can easily be observed.

Figures 10–11 illustrate the 7 different modes that were detected in their chronological order. Note that the phase data and corresponding phase fits typically show greater spatial variation on the inner side of the tokamak (near $\theta = 0^\circ$ or $\theta = 360^\circ$). Table 1 gives the time range which was Fourier analyzed, frequency, Shafranov q value at the edge of the plasma, $\delta B_\theta / B_\theta$, and χ^2_ν for 7 modes. To within the experimental accuracy of $q_s(a)$, it was found that $m/n \leq q_s(a)$. Since $n = 1$ for all 7 modes, the m numbers generally decreased as $q_s(a)$ decreased with time.

Figures 12–13 show the same 7 modes on polar plots. The inner side of the tokamak is to the right of each of the polar plots. The typically increased spatial variation of the mode on the inner side can easily be observed. In Fig. 14 the phases have been negated, shifted relative to the phase of Mirnov coil #1, and added to appropriate multiples of 360° in order to display the phase data from the 7 modes in a more continuous manner. Although λ' is not the same for the 7 modes, a rough $m \sin\theta$ dependence in the toroidal effect can be seen in Fig. 14. This agrees with the $\xi = m\theta + \lambda'(m\sin\theta) + n\phi + \delta_0$ model.

C. Minor Disruptions

Figure 15 depicts two minor disruptions. The first disruption occurred at the end of an $m = 8$, $n = 1$ mode which was quickly followed by an $m = 7$, $n = 1$ mode after a negative loop voltage spike was observed. Later the $m = 7$, $n = 1$ mode grew very large and disrupted, but remained after the negative loop voltage spike. Figure 16 shows I_p , R_p, $q_s(a)$, and $\Lambda = \beta_\theta + l_i/2$ data over the time range in which the two minor disruptions occurred. The growth rates for the first and second modes preceding the two disruptions were estimated from the integrated Mirnov signal to be 900 sec^{-1} and 300 sec^{-1}, respectively. Rough estimates of the Alfvén and resistive time scales of the plasma were made using $R_{mn} = 255\ cm$, $a = 80\ cm$, $n_e = 4 \cdot 10^{12}\ cm^{-3}$, $B_T = 2.8\ T$, and $V_{loop} = 3.5\ V$. For these parameters $\tau_A = 0.084 \cdot 10^{-6}\ sec$ and $\tau_R = 6.5\ sec$, giving a magnetic Reynold's number of $S = \tau_R/\tau_A = 7.7 \cdot 10^7$. Assuming the current profile was such that these modes were unstable, the linear theory[5] predicts a growth rate of $\gamma = \alpha\tau_A^{-2/5}\tau_R^{-3/5}$. Although the growth rate coefficient α depends on the current profile, which is not known, α is on the order of unity and $\tau_A^{-2/5}\tau_R^{-3/5} = 220\ sec^{-1}$.

D. Coupled Modes

Figure 17 shows the Mirnov signal from coil #9 and its Fourier transform. The time range over which the fast Fourier transform was performed on the Mirnov data was from 535–550 ms as is indicated on the graph. Simultaneously existing modes were found with $m = 3$, $n = 1$ and $m = 4$, $n = 1$ at 1.0 and 0.8 kHz, respectively, as indicated on the Fourier transform graph in Fig. 17. Perhaps the relative weakness of the $m = 3$ mode's signal reflects the fact that the $m = 3$ mode lies deeper in the plasma and further away from the Mirnov coils than the $m = 4$ mode. Figure 18 illustrates a superposition of the polar plots from the coupled modes.

E. Electron Diamagnetic Drift Direction

Figure 19 demonstrates two modes rotating in the electron diamagnetic drift direction (v_e^{dia}). The upper three diagrams in Fig. 19 were taken from a different shot (#9031) with the plasma current and toroidal magnetic field reversed, so v_e^{dia} is in the opposite direction. Motion of the mode is essential for Mirnov coils to detect it.

F. Toroidal effect on mode geometry

1. Experiment

A measure of the relative accuracy by which a phase fit approximates the N phase data points is given by *the reduced chi-squared statistic*,[3,7] denoted χ^2. Lower χ^2 values indicate more accurate fits. Minimizing χ^2 is the basis by which the phase parameters m, n, δ_0 and *optionally* λ' *are chosen. The code to implement this minimization actually* evaluates CHI2, where χ^2 =CHI2*3/[(N$-\nu$)π^2], and ν is the number of free parameters in the fit. CHI2 is explicitly defined in Sec. IV.

For the modes which were analyzed in Table 2 it was found that the cylindrical fits ($\lambda' = 0$) approximated the Mirnov phase data poorly. The m, n numbers chosen on the *basis of optimally minimizing* χ^2_{cyl} were inaccurate for all cases in Table 2. Adding the free parameter λ' resulted in better fits as indicated by the $\chi^2_{\lambda'}$ column in Table 2. The optimal choice of m, n, δ_0, λ' *to minimize* $\chi^2_{\lambda'}$ determined the correct m, n numbers of the mode in all cases. Values of $\chi^2_{\lambda'}$ are also given in Table 1, which shows data for the 7 different modes in Figs. 10–14.

Assuming that the mode lies near the outermost (in minor radius) flux surface ($a_p =$ 83 cm, $r_{mn} \approx 80$ cm, $R_c \sim 265$ cm), then $R_{mn} \approx R_p = 255$ cm and one can transform the poloidal angles of the Mirnov coils relative to the vacuum vessel center into poloidal angles relative to the center of the tearing mode (see Fig. 20). R_c and R_p are the major radii of the center of the tokamak vessel and the center of the outermost most flux surface, respectively. This transformation usually improves the accuracy of the subsequently computed toroidal phase fit, as shown under the column headed $\chi^2_{\lambda'_{mode}}$ in Table 2. This improvement reflects the fact that the effect of the mode's off-center position on the phase data can be more *accurately accommodated by a term proportional to* $\sin(\theta)$ *in the coordinates of the mode.* The value of the toroidal correction parameter for the fit using transformed coordinates is given under the column headed λ'_{mode}. This λ'_{mode} value represents the toroidal correction parameter for coordinates relative to the center of the mode if the mode lies near the outermost flux surface.

Again assuming the mode lies near the outermost flux surface, theory[2] predicts that $\lambda = \frac{r_{mn}}{R_{mn}}(\Lambda + 1)$ for $\Lambda = \beta_\theta + l_i/2$ evaluated at the edge of the plasma, and $\lambda'_{mode} \approx \lambda - \frac{y}{m}$. (The $\frac{y}{m}$ *term will be explained in the following section on theory.*) Thus the λ'_{mode} values are expected to be equal to $\lambda'_{Merez} = \frac{r_{mn}}{R_{mn}}(\Lambda + 1) + \frac{y}{m}$ *when the mode lies near the* outermost flux surface. Here values *for* Λ *are measured from the moments* of the external magnetic field. Apparently, from the tabulated data given in Table 2, as $q_s(a)$ decreases, the mode is pushed outward *in minor radius towards the outermost* flux surface so that the assumptions based on the mode's outward position become more valid and $\lambda'_{mode} \rightarrow \lambda'_{Merez}$ for each of the three modes.

2. Theory of Tearing Mode Phase Modulation

The poloidal magnetic field perturbations produced by tearing modes were observed to vary in space more rapidly on the inner side *of the tokamak* ($\theta = 0$). The phase asymmetry is understood to be primarily due to two effects; toroidicity and an off-center position.

In the infinite aspect ratio cylindrical approximation of a tearing mode, a current perturbation of the form $\tilde{j} = j_{mn}\cos(m\theta + n\phi + \delta_0 - \omega t)\delta(r - r_{mn})$, produces variations in the poloidal magnetic field given by[3] $\tilde{B}_r = -A\sin\tilde{\xi}$ and $\tilde{B}_\theta = A\cos\tilde{\xi}$ where

$$A = \frac{\mu_0 j_{mn} r_{mn}}{2}\left(\frac{r_{mn}}{r}\right)^{m+1} \quad , \quad \tilde{\xi} = m\theta + n\phi + \delta_0 - \omega t \quad .$$

The toroidal geometry induces a correction[1-3,6,7] to the mode such that

$$\tilde{\xi} = m\theta^* + n\phi + \delta_0 - \omega t$$

with the "Merezhkin" correction: $\theta^* = \theta + \lambda\sin\theta$

$$\lambda = \lambda(r_{mn}) = \frac{r_{mn}}{R_{mn}}[\beta_\theta(r_{mn}) + \frac{1}{2}l_i(r_{mn}) + 1] \quad .$$

R_{mn} and r_{mn} are the minor and major radii of the m, n flux surface, $\beta_\theta = \frac{8\pi}{B_\theta^2}(\langle p\rangle_{r_{mn}} - p_a)$. $l_i(r_{mn}) = \langle B_\theta^2\rangle_{r_{mn}}/B_\theta^2$, and for any function f, $\langle f\rangle_{r_{mn}} = \int_0^{r_{mn}}\int_0^{2\pi} f(r,\theta)rdrd\theta$.

A secondary effect is due to the fact that the center of the mode and the center of the vacuum vessel do not necessarily *have the same major radius.*[6] *Let* the Grad-Shafranov shift[1] be taken with respect to the outermost flux surface so that $\Delta(r = a) = 0$. Let $s = R_c - R_p$ so that $d = d(r) = s - \Delta(r)$ gives the exact distance by which the flux surface having minor radius r is off-center with respect to the Mirnov coil array. The $\Delta(r)$ term will subsequently be neglected. Figure 20 illustrates the displacement of the outermost flux surface and introduces the variables used to analyze this effect. *The distance* from the vacuum center to the Mirnov coils is $b = 110$ cm. Letting $y = d/b$ one finds that $\gamma = \arcsin[\frac{y\sin\theta}{\sqrt{1 - 2y\cos\theta + y^2}}]$ and $\theta^{mode} = \theta + \gamma$ so that $\theta^* = \theta^{mode} + \lambda\sin\theta^{mode} = \theta + \gamma + \lambda\sin(\theta + \gamma)$.

For a typical TFTR plasma $d = 10$ cm (265 cm − 255 cm) so $y = 1/11$. For TFTR, typically $\Lambda \leq 1$ so that $\lambda \leq \frac{83}{255}(\Lambda + 1) < \frac{2}{3}$. Because the mode is off-centered, the position of each Mirnov coil is an angle of γ away from the orientation which would only measure $\tilde{B}_\theta$ of the mode. In the low frequency limit, the Mirnov coils measure

$$\dot{\tilde{B}} = \dot{\tilde{B}}_\theta \cos\gamma + \dot{\tilde{B}}_r \sin\gamma = \omega A(\sin\tilde{\xi}\cos\gamma + \cos\tilde{\xi}\sin\gamma) = \omega A\sin(\xi)\ ,\ \xi = \tilde{\xi} + \gamma \quad .$$

Fourier analyzing each coil's signal in time gives a phase angle

$$\xi = m\Big[\theta + \arcsin\Big[\frac{y\sin\theta}{\sqrt{1-2y\cos\theta+y^2}}\Big] + \lambda\sin\Big(\theta + \arcsin\Big[\frac{y\sin\theta}{\sqrt{1-2y\cos\theta+y^2}}\Big]\Big)\Big]$$

$$+ \arcsin\Big[\frac{y\sin\theta}{\sqrt{1-2y\cos\theta+y^2}}\Big] + n\phi + \delta_0 - \omega t$$

$$\xi = m[\theta + (\lambda + y + \frac{y}{m})\sin\theta] + n\phi + \delta_0 - \omega t + m\lambda y\cos\theta\sin\theta + O(y^2) \quad .$$

This analysis indicates $\lambda' \approx \lambda + y + \frac{y}{m}$. The same calculation in mode coordinates, using $\gamma = \arcsin(y\sin\theta^{mode})$, yields

$$\xi = m[\theta^{mode} + (\lambda + \frac{y}{m})\sin\theta^{mode}] + n\phi + \delta_0 - \omega t + O(y^3)\ ,\ \lambda'_{mode} \approx \lambda + \frac{y}{m} \quad .$$

Comparison of the phase formulas for physical and mode coordinates reveals that one would expect to obtain lower χ^2 values by converting the physical coordinates into mode coordinates, since this eliminates the $m\lambda y\cos\theta\sin\theta$ term which the fit parameters cannot accommodate. *Transforming to mode coordinates reduces the theoretical errors in the fit from $O(y)$ to $O(y^2)$.* This improvement in the fit was previously verified in the experimental results. It is due to this reduced error that theoretical predictions of the toroidal effect were compared with λ'_{mode} rather than λ'.

The phase angle formula for physical coordinates helps to explain why correct m, n numbers may be obtained by modelling the fit with a free toroidal correction parameter, λ', without having to "worry" about the off-center position of the mode. First of all, the off-center position of the mode typically produces a smaller correction than the dominant Merezhkin correction, *i.e.*, $y + \frac{y}{m} < \lambda$. Secondly, the effect of an off-centered position can be *approximately* accommodated by a term proportional to $\sin\theta$. (The ratio of the maximum effect on the phase fit from the $m\lambda y\sin\theta\cos\theta$ term to the maximum effect of the terms due to the off-center position which are proportional to $\sin\theta$ is $\frac{1}{2}\frac{m}{m+1}\lambda < 1/3$). Thus, the sum of the two effects is allowed for by the free λ' parameter. The tedious computational task of guessing at the effects of toroidicity and the off-centered position on the phase data is consequently unnecessary for analyzing typical TFTR data to obtain correct m, n numbers.

Figure 21 illustrates that for shot #9689 (when the outermost flux surface was displaced from the vacuum center by 10 cm towards the center of the tokamak) the Merezhkin correction dominated the effect of the mode's off-center position. Since $q_s(a) = 6.0$ was measured here, it is assumed that the $m = 6$, $n = 1$ mode is near the edge of the plasma. In Fig. 21 the curved solid line shows the combined effect of the off-center position and the Merezhkin correction. The curved dashed line shows the same radial data plotted against the poloidal angle of the Mirnov coils relative to the center of the mode. Thus the curved *dashed line attempts to isolate the effect of the Merezhkin correction from the effect of* being off-center (neglecting the $\frac{y}{m}$ term since $\frac{y}{m} < y$). This illustrates that for typical TFTR data, the more rapid spatial variation of Mirnov coil phases on the inner side of the tokamak is predominantly due to toroidicity (or the mode's noncylindrical geometry) rather than being caused by the effect of the mode being off-center relative to the array of Mirnov coils. Note for $R_p < R_c$ the two effects enhance each other.

IV. ALGORITHM

The problem of solving for m, n numbers from the Fourier transform phase angles of N Mirnov coil signals taken at a specific frequency is now defined. Let $ph(i)$ denote the phase of the i^{th} Mirnov coil (where $-\pi < ph(i) \leq \pi$). Let $\theta(i)$ and $\phi(i)$ represent the poloidal and toroidal angles giving the position of the i^{th} Mirnov coil relative to the tokamak. The parameters m, n, λ', δ_0 are chosen such that the data, $\{ph(i)\}_{i=1}^{N}$, are best *approximated by the fit*, $\{m[\theta(i) + \lambda' \sin\theta(i)] + n\phi(i) + \delta_0\}_{i=1}^{N}$.

Assume that m, n, λ' are given and one is trying to find the optimal δ_0. δ_0 is determined by minimizing CHI2, the unnormalized chi-squared value of the fit.[8] CHI2 is defined in the following heuristic code, in which $\{y(i)\}_{i=1}^{N} = \{m[\theta(i) + \lambda' \sin\theta(i)] + n\phi(i)\}_{i=1}^{N}$.

```
      FUNCTION CHI2($y, ph, N, \delta_0$)
      CHI2= 0.
      DO 10 i= 1,$N$
      D=ABS($ph(i) - (y(i) + \delta_0)$)
      D=AMOD(D+$\pi$,2$\pi$) - $\pi$          ! *
10    CHI2=CHI2+D*D
      RETURN
```

Excluding the step followed by an asterisk, CHI2$= \sum_{i=1}^{N} (ph(i) - y(i) - \delta_0)^2$. The "asterisk step" essentially adds 2π times an integer to the difference between the actual phase and the phase fit, so that D$\leq \pi$. Two signals cannot be more than 180° out of phase, and adding any integer times 2π to a phase does not change the signal it represents.

δ_0 could be solved for by applying a "grid search" followed by an iterative minimization routine using the CHI2 function with δ_0 restricted to lie within any 2π interval. In order to determine m and n this minimization algorithm is placed within two nested DO loops, which test each m, n combination and minimize CHI2=CHI2(m, n, δ_0) with λ' given. The resulting minimum CHI2 value defines CHI2(λ'), and (if desired) the optimum λ' value may be determined by applying a "search and iterate" routine to this CHI2(λ') function. Analysis of Mirnov data may typically involve running this four parameter search algorithm very often. Since the algorithm to determine δ_0 is nested within loops to determine m, n and λ', it would be beneficial to speed up the method of solving for δ_0, given m, n, λ'.

An analytical method was developed to find the value of δ_0 which will minimize CHI2(δ_0) with m, n, λ' given. It can best be described by defining an equivalent norm, CHINEW(δ_0). Let

$$r(i) = ph(i) - \{m[\theta(i) + \lambda' \sin\theta(i)] + \phi(i)\} \quad . \tag{1}$$

Let $\{t(i)\}_{i=1}^{N}$ be the sequence $\{r(i)\}_{i=1}^{N}$ with each element mapped into the interval $[-\pi, \pi]$ by adding 2π times an integer. Let $\{W_0(i)\}_{i=1}^{N}$ be the $\{t(i)\}_{i=1}^{N}$ sequence rearranged in ascending order. Now CHI2(δ_0) =CHI2(y, ph, n, δ_0) may be defined equivalently in terms of the $\{W_0(i)\}_{i=1}^{N}$ sequence.

```
          FUNCTION CHINEW(W₀,N,δ₀)
          CHINEW= 0.
          DO 10 i= 1,N
          D=ABS(W₀(i) - δ₀)
          D=AMOD(D+π,2π) - π             ! *
      10  CHINEW=CHINEW+D*D
          RETURN
```

Note CHINEW(W_0, N, δ_0) =CHI2(δ_0). Note if $\delta_0 \in [W_0(N) - \pi, W_0(1) + \pi]$, then the "asterisk step" has no effect, CHINEW= $\sum_{i=1}^{N} (W_0(i) - \delta_0)^2$, and by standard analysis, $\delta_0 = \frac{1}{N} \sum_{i=1}^{N} W_0(i) = \overline{W_0}$ is a critical point of CHINEW.

Define another sequence, $\{W_1(i)\}_{i=1}^{N} = \{W_0(2), W_0(3), \ldots, W_0(N), W_0(1) + 2\pi\}$. The elements of $\{W_1(i)\}_{i=1}^{N}$ are in ascending order. Note CHINEW(W_1, N, δ_0) =CHI2(δ_0). Note if $\delta_0 \in [W_0(1) + \pi, W_0(2) + \pi]$, then the "asterisk step" has no effect, CHINEW= $\sum_{i=1}^{N} (W_1(i) - \delta_0)^2$, and by standard analysis $\delta_0 = \frac{1}{N} \sum_{i=1}^{N} W_1(i) = \overline{W_0} + \frac{2\pi}{N}$ is a critical point.

Define the next sequence, $\{W_2(i)\}_{i=1}^{N} = \{W_0(3), \ldots, W_0(N), W_0(1) + 2\pi, W_0(2) + 2\pi\}$. The elements of $\{W_2(i)\}_{i=1}^{N}$ are in ascending order. Note CHINEW(W_2, N, δ_0) =CHI2(δ_0).

Note if $\delta_0 \in \left[W_0(2)+\pi, W_0(3)+\pi\right]$, then the "asterisk step" has no effect, CHINEW= $\sum_{i=1}^{N}\left(W_2(i)-\delta_0\right)^2$, and by standard analysis $\delta_0 = \frac{1}{N}\sum_{i=1}^{N} W_2(i) = \overline{W_0} + \frac{4\pi}{N}$ is a critical point.

Continuing to add 2π to the first and least element of the previous ascending W_k sequence and transferring the result to the last (and greatest) element of the W_{k+1} sequence generates N critical points over a 2π interval (or domain) for δ_0. The critical points are $\left\{c_k\right\}_{k=0}^{N-1} = \left\{\overline{W_0}+\frac{2\pi k}{N}\right\}_{k=0}^{N-1}$. It has been rigorously proven that the optimal δ_0 is in this set of critical points and if $\delta_0 = c_k$ is optimal, then $\mathrm{CHI2}(y, ph, N, c_k) = \sum_{i=1}^{N}\left(W_k(i)-c_k\right)^2$.

Generating the sequence $\left\{H_k\right\}_{k=0}^{N-1} = \left\{\sum_{i=1}^{N}\left(W_k(i)-c_k\right)^2\right\}_{k=0}^{N-1}$ may be simplified by substituting for c_k and the W_k's in terms of the W_0's. A recurrence relation useful for determining the smallest element of the sequence, $\left\{H_k\right\}_{k=0}^{N-1}$, may then be derived. Substituting $c_k = \overline{W_0} + \frac{2\pi k}{N}$ and $\sum_{i=1}^{N} W_0(i) = N\overline{W_0}$ into

$$H_k = \sum_{i=1}^{k}\left[W_0(i)+2\pi-c_k\right]^2 + \sum_{i=k+1}^{N}\left[W_0(i)-c_k\right]^2$$

$$\text{and letting} \quad S_k = \frac{1}{4\pi}\left[H_k - \sum_{i=1}^{N} W_0^2(i) - N(\overline{W}_0)^2\right] \quad . \tag{2}$$

one finds that $S_0 = 0$ and for $k > 0$,

$$S_k = W_0(k) - \overline{W_0} + \frac{2\pi}{N}\left(\frac{N+1}{2} - k\right) + S_{k-1} \quad . \tag{3}$$

Finding j such that

$$S_j = \min_{0 \le k \le N-1} S_k$$

determines the optimal δ_0, *i.e.*, $\delta_0 = c_j$. The code to implement this algorithm for determining m, n, δ_0 for a given λ' is given in the appendix.

The described algorithm was used to define $\mathrm{CHI2}(\lambda')$ which minimizes CHI2 with respect to m, n, δ_0. The described algorithm was also used to minimize CHI2 with respect to all four parameters, m, n, δ_0, λ'. $\mathrm{CHI2}(\lambda')$ was evaluated at 32 equally spaced points over the region of interest, $(-1 \le \lambda' \le 1)$, to constrict the neighborhood containing the absolute minima. This prevented the subsequent iterative minimization routine from converging to any relative minima other than the absolute minima.

Another method of minimizing CHI2 with respect to all four parameters was devised. Rather than applying a search and standard iterative minimization routine using $\mathrm{CHI2}(\lambda')$

to determine the optimal m, n, δ_0, λ', a much more sophisticated code was developed to find *both* λ' and δ_0 analytically. For large N and a fixed range of m, n numbers the more sophisticated algorithm's run time scaled as N^3 and the described iterative approach scaled as N^2. Unfortunately, for TFTR data ($N = 19$ Mirnov coils) the sophisticated analytical algorithm ran only slightly faster than the iterative algorithm when allowing a 0.00001 error in λ'. For the algorithm which obtained both λ' and δ_0 analytically, the added complexity and 200 lines of FORTRAN code required did not seem to be justified.

A second method for finding both λ' and δ_0 analytically exists. This optional method was not used to analyze the Mirnov data. Unlike the method described in the preceding paragraph, this method is not certain to provide the correct answer when one or more "bad" data points are approximately 180° away from the optimal phase fit. This method involves iteratively minimizing CHI2(λ') until one has determined the m, n numbers and has a good approximation of what λ' and δ_0 are. Let the parameters obtained at the end of this iterative minimization procedure be $(m_g, n_g, \delta_g, \lambda'_g)$. Let $s(\delta_0, \lambda', i) = [m_g(\theta(i) + \lambda' \sin\theta(i)) + n_g\phi(i) + \delta_0 - \tilde{ph}(i)]^2$ where $\tilde{ph}(i)$ is the value of $ph(i)$ summed with the appropriate multiple of 2π to make $s(\delta_0 = \delta_g, \lambda' = \lambda'_g, i) \le \pi^2$. Letting

$$f = f(\delta_0, \lambda') = \sum_{i=1}^{N} s(\delta_0, \lambda', i) \qquad ,$$

the optimal values of λ' and δ_0 are then found by setting

$$\frac{\partial f}{\partial \delta_0} = \frac{\partial f}{\partial \lambda'} = 0 \qquad .$$

The resulting parameters are $m = m_g$, $n = n_g$ and with $x(i) = -\tilde{ph}(i) + m\theta(i) + n\phi(i)$,

$$A = \sum_{i=1}^{N} x(i) \ , \ B = \sum_{i=1}^{N} x^2(i) \ , \ C = \sum_{i=1}^{N} \sin\theta(i) \ , \ D = \sum_{i=1}^{N} \sin^2\theta(i) \ , \ E = \sum_{i=1}^{N} x(i)\sin\theta(i) \ ,$$

one obtains

$$\begin{pmatrix} \delta_0 \\ m\lambda' \end{pmatrix} = \frac{1}{DN - C^2} \begin{pmatrix} CE - AD \\ AC - EN \end{pmatrix}$$

and for these parameters, CHI2 $= f = B + Em\lambda' + A\delta_0$. An advisable precaution would be to use this method to terminate the CHI2(λ') minimization iteration only if this method yields the same answer when $(m_g, n_g, \delta_g, \lambda'_g)$ are set to the values corresponding to the minimum and maximum values within which λ' has been restricted to lie.

V. CONCLUSION

The methods presented for constructing phase fits and polar plots significantly improved the accuracy of mode number determination from Mirnov coil data. It was found that making a proper fit to the phase data required a correction parameter, λ', to accommodate the effects of the toroidicity and the off-center position of the mode. Improved resolution of mode geometry was made possible through better data analysis techniques so that modes with m numbers as high as $m = 9$ can be clearly seen on the various plots presented.

Interesting physical phenomena occurring during the start-up of shot #9689 were observed. As the mode numbers evolved from higher to lower m numbers, seven different modes with $n = 1$ and m numbers from $m = 9$ to $m = 3$ were detected. A correlation between m/n and $q_s(a)$ was observed. Minor disruptions were preceded by growing modes. Simultaneously existing modes were found with $m = 4$, $n = 1$ and $m = 3$, $n = 1$. The modes detected on shot #9689 and other shots consistently rotated in the electron diamagnetic direction. More analysis of Mirnov coil data would be useful to see if the physical phenomena seen on shot #9689 are typical.

Mirnov data from the different modes were used to construct polar plots which clearly displayed increased spatial variation on the inner side of the tokamak. Placing relatively more Mirnov coils on the inner side of the machine should be considered for future machine designs in order to enhance mode resolution and the detection of high m numbers. The effect of toroidicity typically dominates the effect due to the mode's off-center position for TFTR data. Theoretical calculations from Merezhkin[2] on this toroidal effect were tested and found to be consistent with the data.

Anyone who wishes to obtain m, n numbers from phase correlation analysis could benefit from the algorithm which was developed for that purpose. The difficulties in estimating the value of λ' were circumvented by using the computer to find λ' automatically. The improved efficiency of the algorithm reduces run time greatly and significantly enhances the ease of between-shot analysis requiring m, n number calculation.

ACKNOWLEDGMENTS

The author wishes to thank Gregory Hammett for many helpful discussions. This work was supported by U.S. Department of Energy Contract No. DE-AC02-76-CHO-3073.

APPENDIX

```
C——Heuristic code to determine m,n,δ0 for a given λ'
C——and return the resulting CHI2(λ') value
      FUNCTION CHI2(ph,θ,φ,λ',MLOW,MHI,NLOW,NHI,   m,n,δ0)
      R=FLOAT(N+1)/2.
      Q= 2π/FLOAT(N)
      DO 5 i = 1,N
5     SI(i) = sin(θ(i))
      CHI2= 10000.
      DO 30 M1=MLOW,MHI
      DO 30 N1=NLOW,NHI
      WSUM= 0.
      WWSUM= 0.
      DO 10 i = 1,N
      W(i) = ph(i)-FLOAT(M1)*(θ(i) + λ'*SI(i))-FLOAT(N1)*φ(i))       ! (see eqn.1)
      Z= π
      IF(W(i).LT.0.)Z= -π
      W(i) =AMOD(W(i)+Z, 2π)-Z
      WSUM=WSUM + W(i)
10    WWSUM=WWSUM+W(i)*W(i)
      WAVG=WSUM/FLOAT(N)
C——Subroutine ORDER arranges the W array in ascending order
      CALL ORDER(W,N)
      S= 0.
      SBEST=S
      j= 0
      DO 20 k = 1,N-1
      SNEXT=W(k)-WAVG+Q*(R-FLOAT(k))+S                                ! (see eqn.3)
      IF(SNEXT.GE.SBEST) GOTO 20
      SBEST=SNEXT
      j= k
20    S=SNEXT
      CHI= 4π*SBEST+WWSUM-WSUM*WAVG                                   ! (see eqn.2)
      IF(CHI.GE.CHI2) GOTO 30
      CHI2=CHI
      δ0 =WAVG+ Q*FLOAT(j)
      m =M1
      n =N1
30    CONTINUE
      RETURN
```

If desired, one could further optimize the program by setting up arrays PHN1(i,N1-NLOW+1)=$\phi(i)$*FLOAT(N1), THM1(i,M1-MLOW+1)= $\theta(i)$*FLOAT(M1), and SINM1(i,M1-MLOW+1) = sin($\theta(i)$)*FLOAT(M1). Passing PHN1, THM1, SINM1, R, and Q to FUNCTION CHI2 through a common block would then enable the W array to be initialized with less multiplication and reduce needless redundancy in the computation, (especially if FUNCTION CHI2 is called more than once). Note minor modifications of this code would be required for a FORTRAN compiler, *i.e.*, $\pi, \theta, \phi, \delta_0$, and λ' need new names and EXTERNAL, DIMENSION, and COMMON statements should be included. The IMSL Library[9] provides a routine called VRSTA which arrange arrays in ascending order.

REFERENCES

1. V. D. Shafranov, *Reviews of Plasma Physics* [2] The Consultants Bureau, New York, (1969) 103.
2. V. G. Merezhkin, Sov. J. Plasma Phys. **4** (2) (1978) 152.
3. G. Hammett and K. McGuire, Princeton Plasma Physics Lab. Rep. PPPL-1854, 15 (1982).
4. R. S. Granetz, I. H. Hutchinson, D. O. Overskei, Nuclear Fusion **19** (3) (1979) 1587.
5. R. B. White, "Resistive Instabilities and Field Line Reconnection." In Vol. 1 of *Basic Plasma Physics*, edited by A. A. Galeev and R. N. Sudan, North Holland Publishing Co., New York, (1983) p.632–633.
6. L. C. J. M. DeKock, B. J. H. Meddens, L. T. M. Ornstein, D. C. Schram, R. J. J. Van Heijningen, Massachusetts Institute of Technology Rep. PRR-7414 (1974).
7. G. Fussman, B. J. Green, H.P. Zehrfeld, *Plasma Physics and Controlled Nuclear Fusion Research* (Proc. Int. Conf. Brussels, 1980).
8. Phillip R. Bevington, *Data Reduction and Error Analysis for the Physical Sciences*, McGraw-Hill, New York, (1969).
9. IMSL Inc., *The IMSL Library Edition 9 Reference Manual* [2], International Mathematical and Statistical Libraries, Inc., Houston, (1982).

Table 1.

time range (ms)	freq (kHz)	m, n	$q_s(a)$	$\delta B_\theta / B_\theta$ %	$\chi^2_{\lambda'}$
85–90	1.4	9, 1	9.3	0.057	0.193
120–130	1.1	8, 1	7.8	0.055	0.065
190–200	0.8	7, 1	6.8	0.152	0.059
285–290	1.5	5, 1	6.3	0.021	0.062
382–387	1.2	6, 1	6.0	0.052	0.048
530–535	1.2	3, 1	5.5	0.062	0.033
540–550	0.8	4, 1	5.4	0.126	0.016

Table 2.

time range (ms)	freq (kHz)	m, n	$q_s(a)$	$\delta B_\theta / B_\theta$ %	$\chi^2_{\lambda'}$	$\chi^2_{\lambda'_{mode}}$	λ'_{mode}	λ'_{Merez}
107-111	2.0	8, 1	8.3	0.037	0.111	0.100	0.368	0.443
120-130	1.1	8, 1	7.8	0.055	0.065	0.045	0.432	0.445
135-138	1.7	8, 1	7.5	0.057	0.132	0.113	0.438	0.442
145-150	1.2	7, 1	7.2	0.085	0.127	0.135	0.323	0.441
190-200	0.8	7, 1	6.8	0.152	0.059	0.039	0.460	0.458
210-220	0.7	7, 1	6.7	0.149	0.066	0.051	0.484	0.467
330-335	1.4	6, 1	6.2	0.075	0.054	0.045	0.436	0.469
340-350	1.1	6, 1	6.1	0.106	0.052	0.043	0.450	0.483
382-387	1.2	6, 1	6.0	0.052	0.048	0.038	0.472	0.491

FIGURE CAPTIONS

Fig. 1 Locations of Mirnov coils in TFTR.

Fig. 2 Examining a Mirnov signal from shot #9689 reveals a region of interest (a), which is expanded and compared with the signals from the poloidal array of the first 16 Mirnov coils (b).

Fig. 3 This figure shows how the data shown in Fig. 2 are analyzed. Each signal is Fourier analyzed from 340–350 ms and each signal's Fourier spectrum of amplitudes is averaged together (a). The phases from each coil at 1.1 kHz are shown in (b). The data points from coils 17–19 are usually denoted by a distinctive symbol in this report. The term $n[\phi(1) - \phi(i)]$ *is added to the phases from coils 17–19 in order to compare their phases with the poloidal array which is at a different toroidal angle. This term comes from the* ϕ *dependence in the* $\xi = m(\theta + \lambda' \sin\theta) + n\phi + \delta_0$ *model. Thus an* $n = 1$ *number was assumed a priori in (b) in order to plot the data from coils 17–19. The phase data in (b) are correlated by an optimal cylindrical fit (c). An optimal toroidal fit (d), in which* λ' *is chosen to optimize the fit, is also shown.*

Fig. 4 The dashed line indicates the optimal cylindrical fit to a typical $m = 4$ *mode's phase data. The cylindrical fit "wraps around" from bottom to top 3 times, indicating* $m = 3$*. The optimal toroidal fit correctly indicates* $m = 4$.

Fig. 5 Four different ways of analyzing the same set of phase data are illustrated. The cylindrical fit (a) indicates $m = 4$*. Interpolating* $\{\theta(i), r(i) = a(i)\cos[ph(i)] + C\}_{i=1}^{N}$ *with a cubic spline (b) indicates* $m = 5$*. The optimal toroidal fit (c) correctly indicates* $m = 6$*. Careful analysis of the* $m = 6$ *corrected polar plot (d) reveals that a branch of the mode was missed in (b). The location of this branch is indicated by an arrow in (b).*

Fig. 6 The phase data in (a) from an $m = 6$ *mode are adjusted by adding appropriate multiples of 360° in order to illustrate the optimal cylindrical and toroidal fits in a continuous manner. The optimal toroidal fit is adjusted to interpolate the phase data by adding the cubic spline shown in (b). A cubic spline of the amplitude data taken from each coil at the same frequency is shown in (c). These cubic splines have matching* 0^{th}, 1^{st}, *and* 2^{nd} *derivatives at* $\theta = 0°$ *and* $\theta = 360°$ *and were calculated by IMSL*[9] *routine ICSPLN. The corrected polar plot which (b) and (c) were used to produce is shown in (d). The same polar plot data against* $\theta' = \theta + \lambda' \sin\theta$ *(instead of* θ*) are shown in (e).*

Fig. 7 Parameters of shot #9689 during start-up including $\Lambda = \beta_\theta - l_i/2$, R_p, I_p, *and* $q_\psi(a)$.

Fig. 8 Line-averaged density of shot #9689 during start-up.

Fig. 9 A summary of the mode evolution during start-up on shot #9689 is shown with the Mirnov signal from coil #9.

Fig. 10–11 Phase data from 7 of the modes detected during start-up are illustrated. Additional data for these 7 modes are shown in Table 1. The 7 modes in Figs. 10–11, Figs. 12–13, Fig. 14 and Table 1 were each taken from the same time range and frequency.

Fig. 12–13 Polar plots for the 7 detected modes. Although $m = 9$ is above the Nyquist limit for 16 evenly spaced Mirnov coils, the 3 other coils remove the "degeneracy" between the $m = 9$ and $m = -7$ modes. For the phase data of the given $m = 9$ mode, $\chi^2_{\lambda'}(m = 9, n = 1) = 0.193 < \chi^2_{\lambda'}(m = -7, n = 1) = 0.241$.

Fig. 14 The phases from the 7 modes have been negated and shifted by appropriate multiples of 360° in order to show the data and their optimal toroidal phase fits in a continuous manner.

Fig. 15 The effects of disruptive plasma behavior in the Mirnov coil and loop voltage signals during shot #9689.

Fig. 16 Parameters of the plasma during the disruptive activity shown in Fig. 15.

Fig. 17 Simultaneous $m = 3$ and $m = 4$ modes were detected at 1.0 kHz and 0.8 kHz, respectively.

Fig. 18 Polar plot for the simultaneous $m = 3$ and $m = 4$ modes.

Fig. 19 The lower 3 diagrams illustrate an $m = 3$ mode rotating with time in the electron diamagnetic drift direction during shot #9689. The upper 3 diagrams show an $m = 3$ mode's motion during another shot (#9031) with the electron diamagnetic drift direction reversed.

Fig. 20 This picture illustrates the variables used to analyze the effect of the mode's off-center position on the phase data. The transformation from coordinates taken with respect to the vacuum vessel to coordinates relative to the center of the mode is derived from $\theta^{mode} = \theta + \alpha$ and $\sin\alpha/d = \sin\theta/\sqrt{b^2 + d^2 - 2bd\cos\theta}$.

Fig. 21 The curved solid line indicates the polar plot of the actual data. The asymmetrically increased spatial variation in the phase data on the inner side of the tokamak is caused by toroidal effects and the off-center position of the mode relative to the vacuum vessel center. The dashed line shows the same radial data with the poloidal coordinates taken relative to the center of the mode, thus attempting to remove the effect due to the off-center position. Since the dashed outline of the mode shows that the noncylindrical asymmetry of the mode is only slightly reduced, it illustrates that the toroidal effect dominates the effect due to the mode's off-center position.

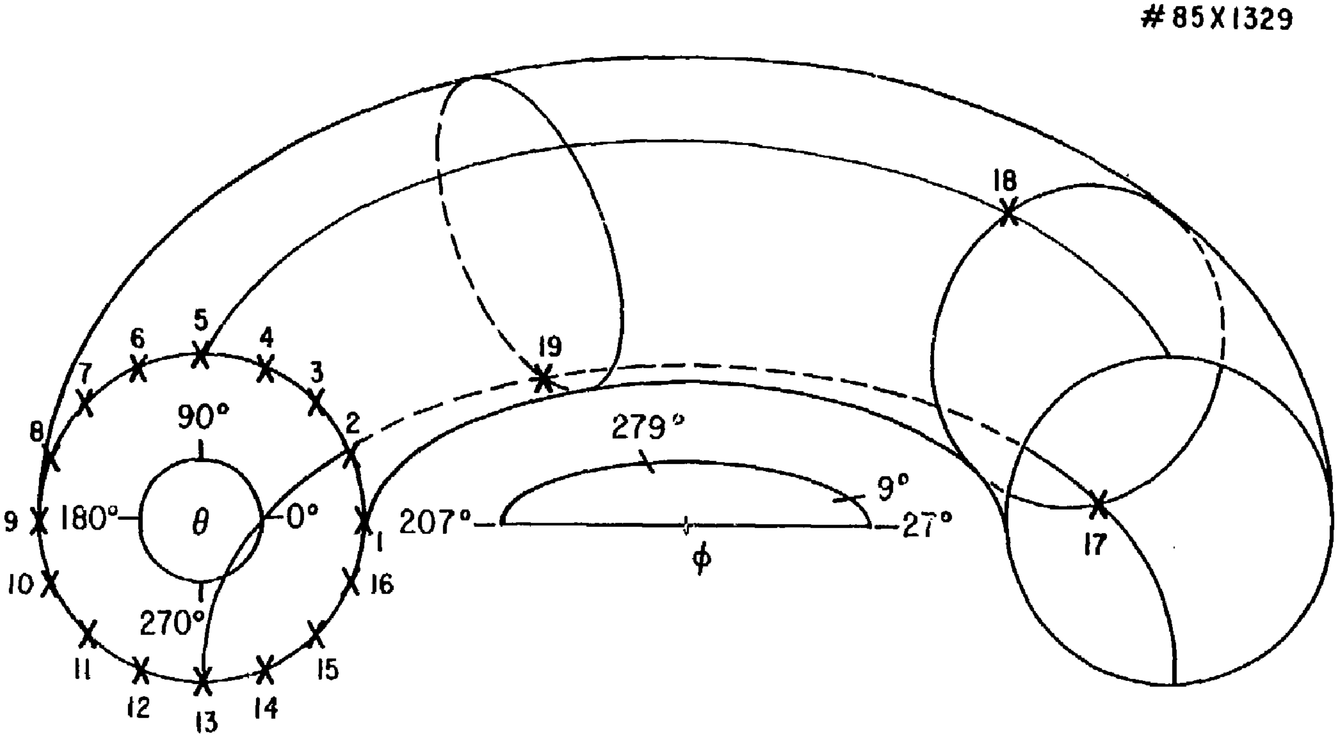
#85X1329
19
18
17
1
2
3
4
5
6
7
8
9
10
11
12
13
14
15
16
90°
180°
0°
270°
θ
279°
9°
207°
27°
ϕ

Fig. 1

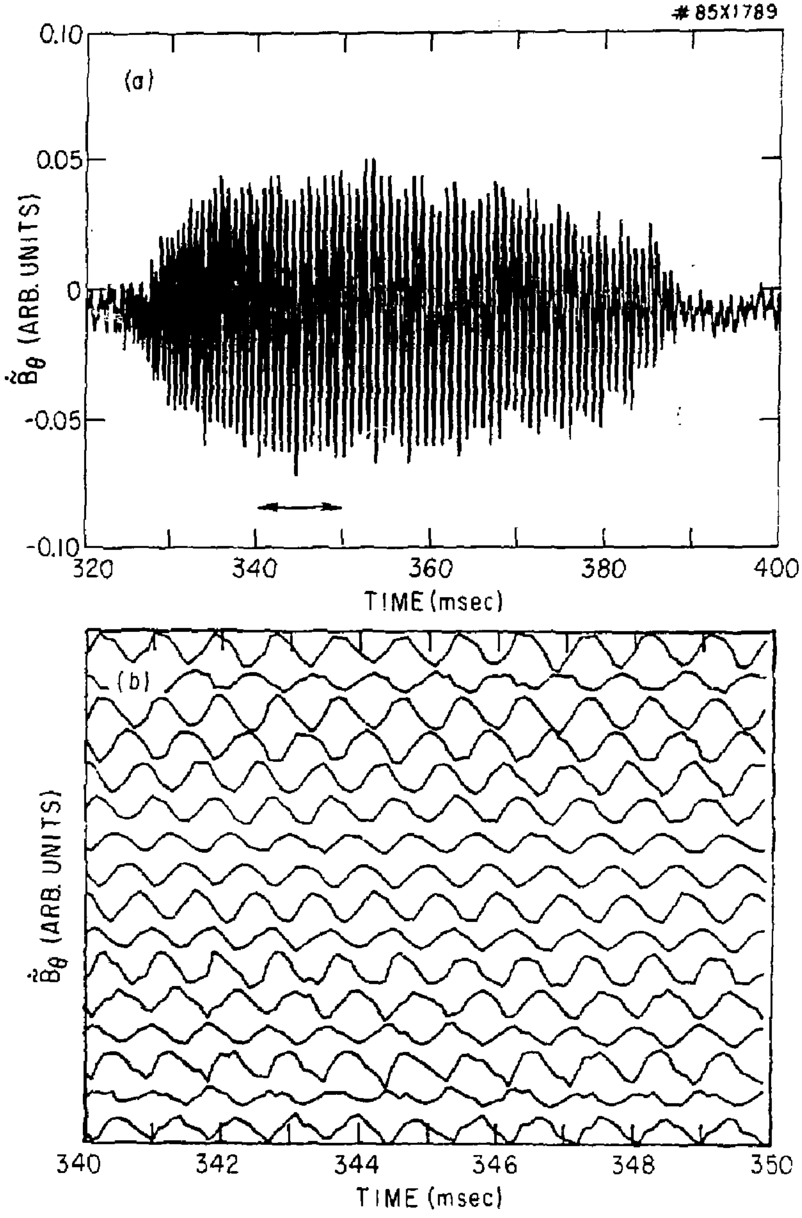
#85X1789
(a)
0.10
0.05
0
-0.05
-0.10
$\dot{\tilde{B}}_\theta$ (ARB. UNITS)
320
340
360
380
400
TIME (msec)
(b)
$\dot{\tilde{B}}_\theta$ (ARB. UNITS)
340
342
344
346
348
350
TIME (msec)

Fig. 2

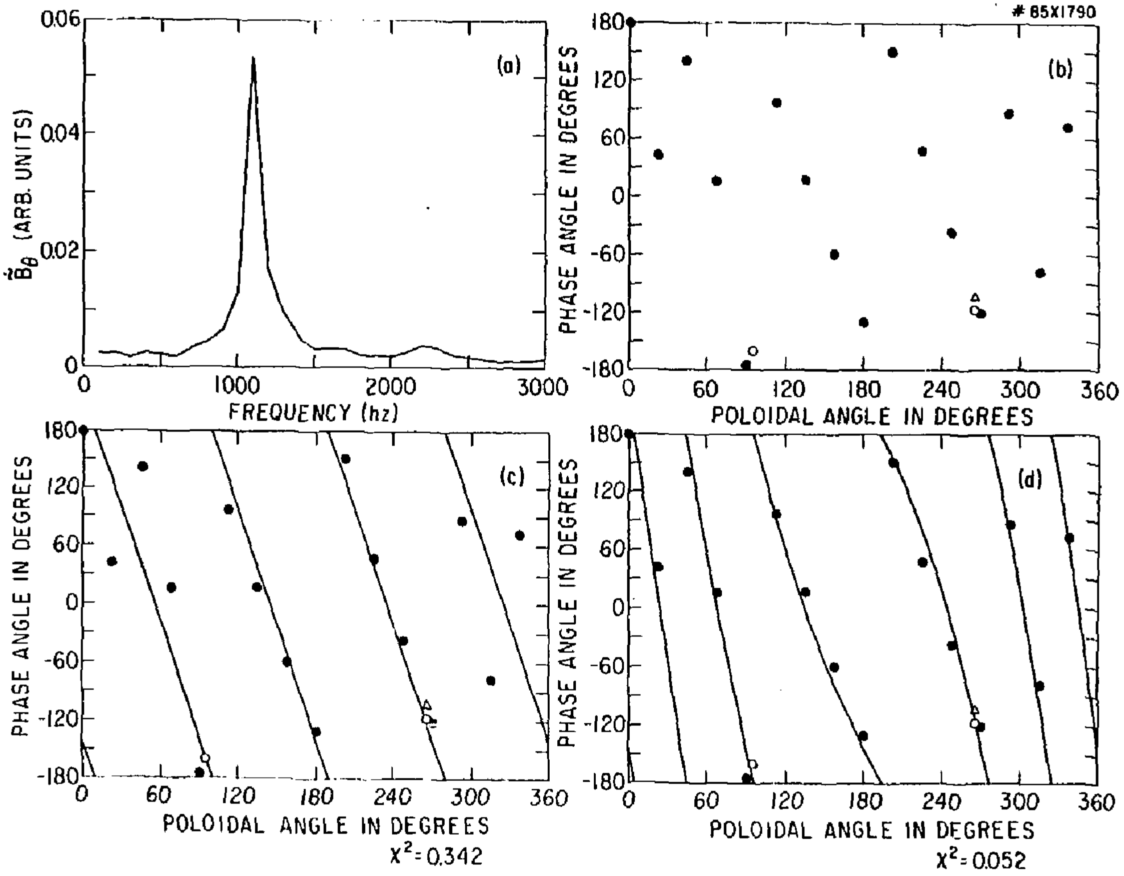
#85X1790
(a)
$\tilde{\dot{B}}_\theta$ (ARB. UNITS)
0.06
0.04
0.02
0
0
1000
2000
3000
FREQUENCY (hz)
(b)
PHASE ANGLE IN DEGREES
180
120
60
0
-60
-120
-180
0
60
120
180
240
300
360
POLOIDAL ANGLE IN DEGREES
(c)
PHASE ANGLE IN DEGREES
POLOIDAL ANGLE IN DEGREES
X^2=0.342
(d)
PHASE ANGLE IN DEGREES
POLOIDAL ANGLE IN DEGREES
X^2=0.052

Fig. 5

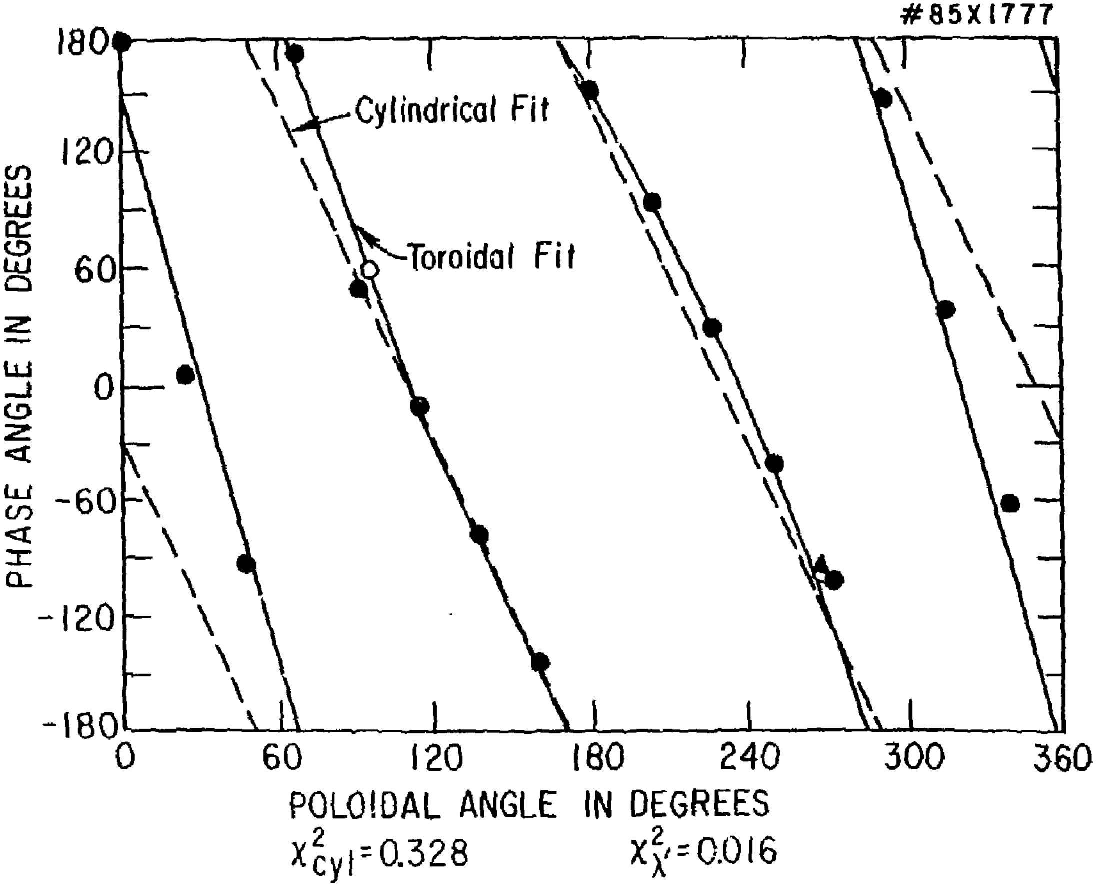
#85X1777
Cylindrical Fit
Toroidal Fit
PHASE ANGLE IN DEGREES
180
120
60
0
-60
-120
-180
POLOIDAL ANGLE IN DEGREES
0
60
120
180
240
300
360
$\chi^2_{cyl} = 0.328$
$\chi^2_{\chi'} = 0.016$

Fig. 4

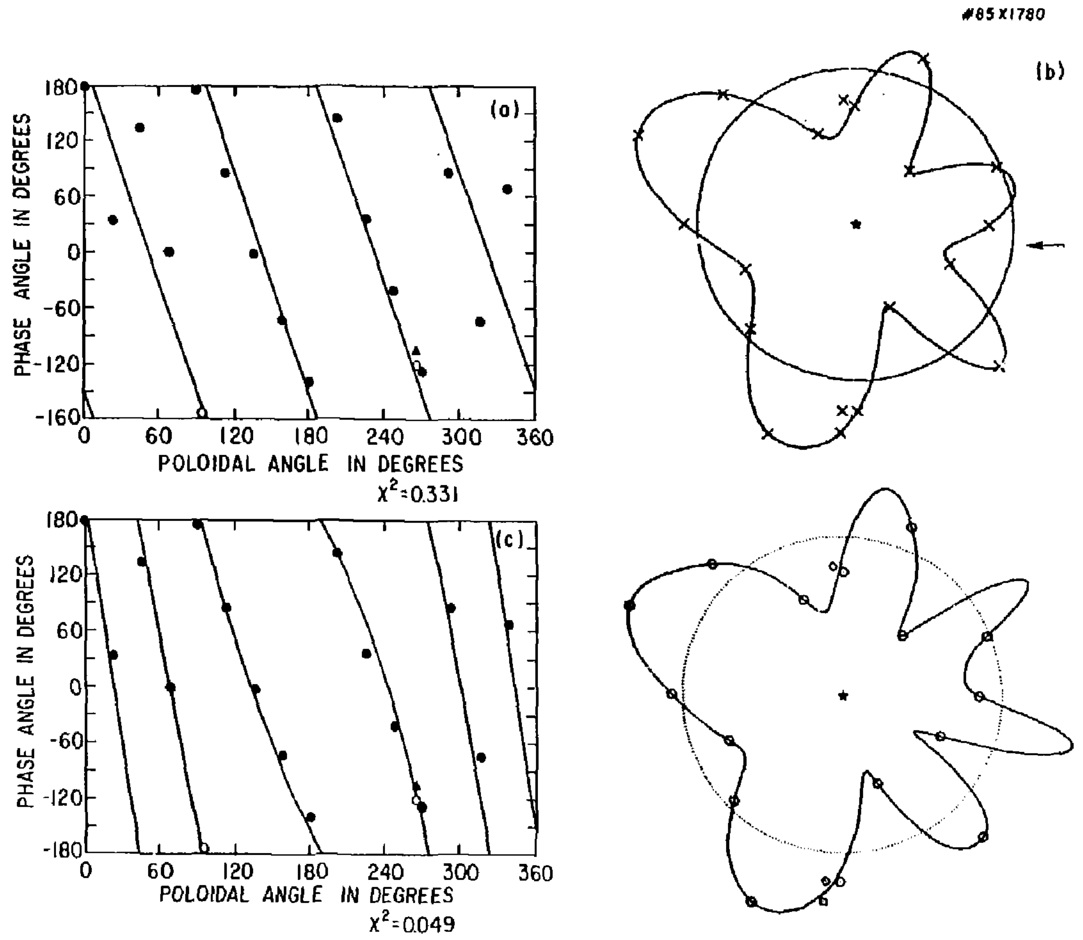
#85X1780
(a)
(b)
(c)
PHASE ANGLE IN DEGREES
180
120
60
0
-60
-120
-160
-180
POLOIDAL ANGLE IN DEGREES
0
60
120
180
240
300
360
χ^2=0.331
χ^2=0.049

Fig. 5

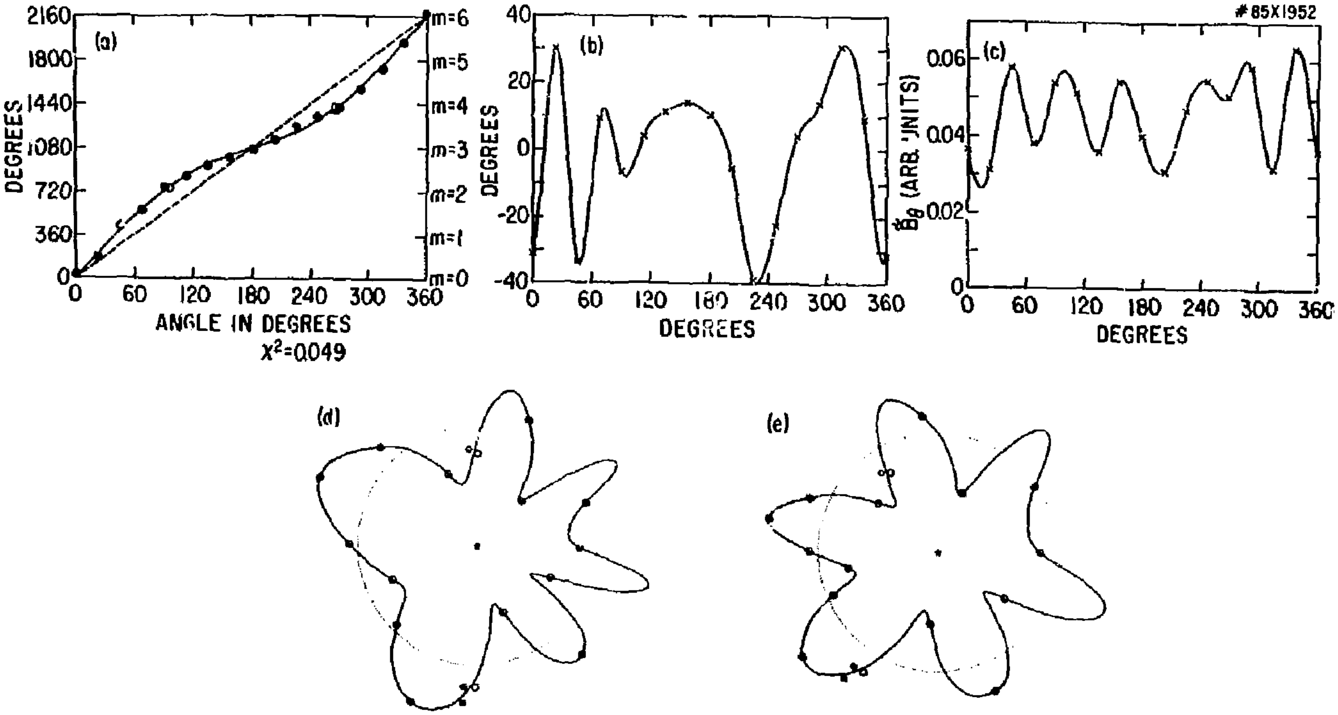
#85X1952
(a)
DEGREES
2160
1800
1440
1080
720
360
0
m=6
m=5
m=4
m=3
m=2
m=1
m=0
0
60
120
180
240
300
360
ANGLE IN DEGREES
χ^2=0.049
(b)
DEGREES
40
20
0
-20
-40
0
60
120
180
240
300
360
DEGREES
(c)
$\tilde{B}_\theta$ (ARB. UNITS)
0.06
0.04
0.02
0
0
60
120
180
240
300
360
DEGREES
(d)
(e)

Fig. 6

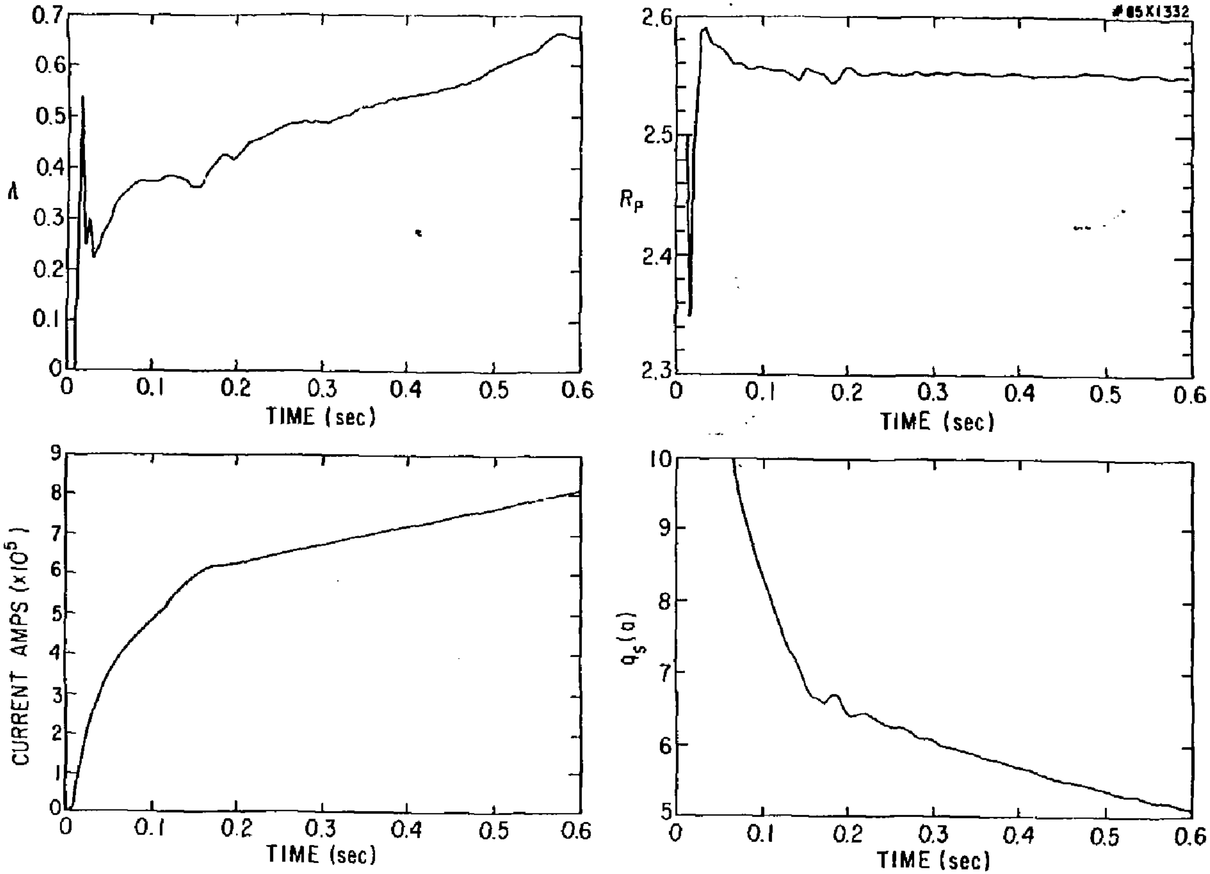
#85X1332
Λ
0.7
0.6
0.5
0.4
0.3
0.2
0.1
0
0
0.1
0.2
0.3
0.4
0.5
0.6
TIME (sec)
R_p
2.6
2.5
2.4
2.3
0
0.1
0.2
0.3
0.4
0.5
0.6
TIME (sec)
CURRENT AMPS ($\times 10^5$)
9
8
7
6
5
4
3
2
1
0
0
0.1
0.2
0.3
0.4
0.5
0.6
TIME (sec)
$q_s(a)$
10
9
8
7
6
5
0
0.1
0.2
0.3
0.4
0.5
0.6
TIME (sec)

Fig. 7

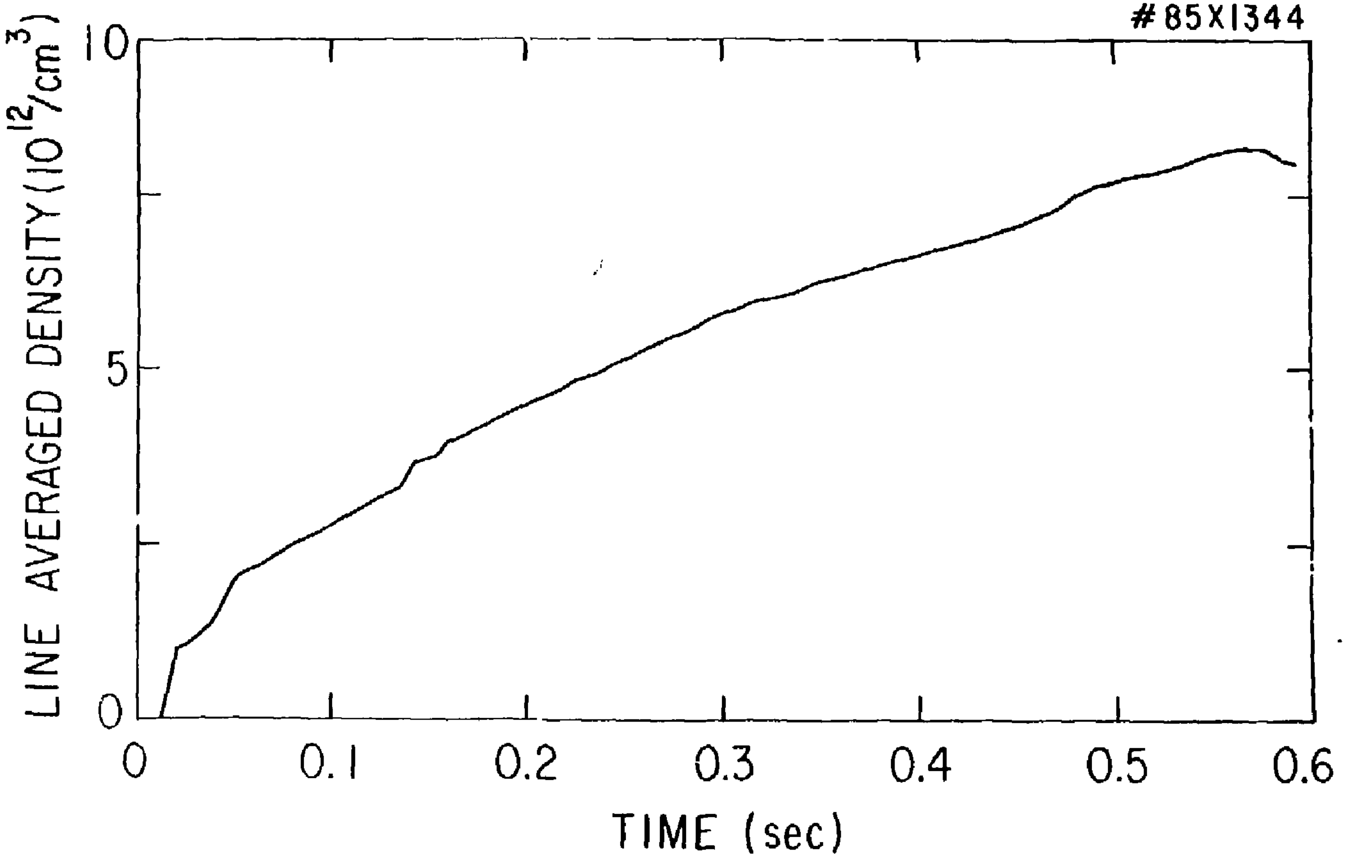
#85X1344
LINE AVERAGED DENSITY (10^{12}/cm^3)
0
5
10
0
0.1
0.2
0.3
0.4
0.5
0.6
TIME (sec)

Fig. 8

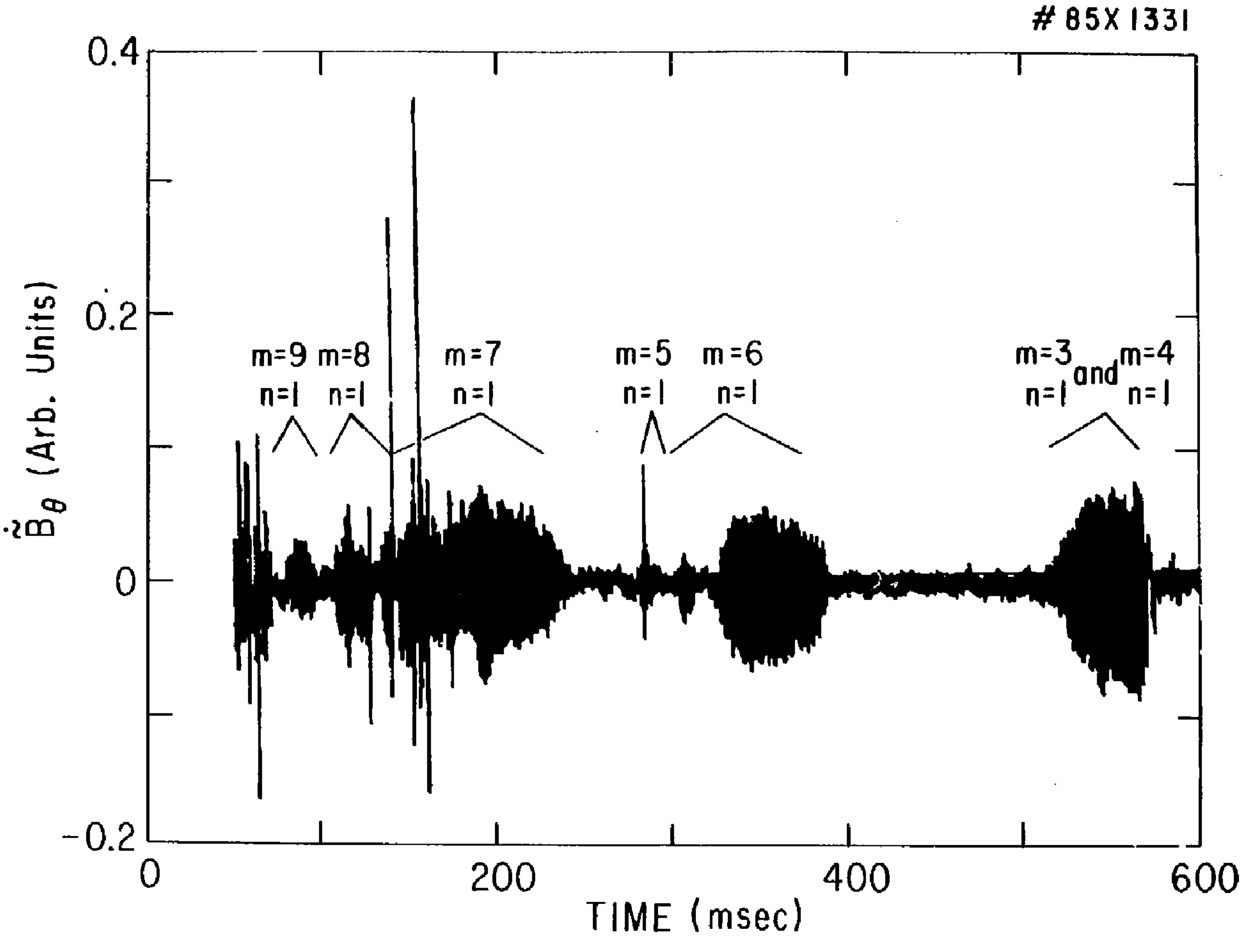

85X 1331
0.4
0.2
0
−0.2
$\tilde{\dot{B}}_\theta$ (Arb. Units)
0
200
400
600
TIME (msec)
m=9 n=1
m=8 n=1
m=7 n=1
m=5 n=1
m=6 n=1
m=3 n=1 and m=4 n=1

Fig. 9

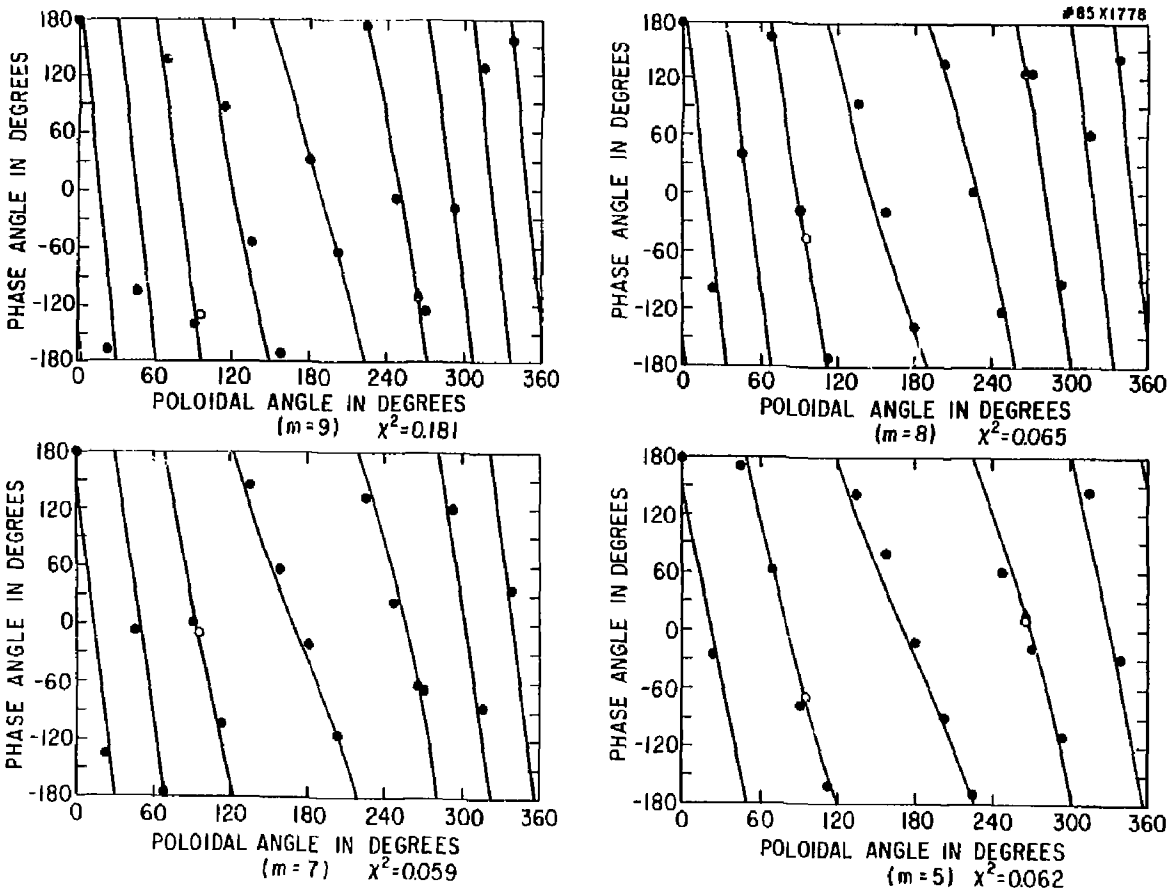
#85X1778
PHASE ANGLE IN DEGREES
180
120
60
0
-60
-120
-180
POLOIDAL ANGLE IN DEGREES
0
60
120
180
240
300
360
(m=9) χ^2=0.181
(m=8) χ^2=0.065
(m=7) χ^2=0.059
(m=5) χ^2=0.062

Fig. 10

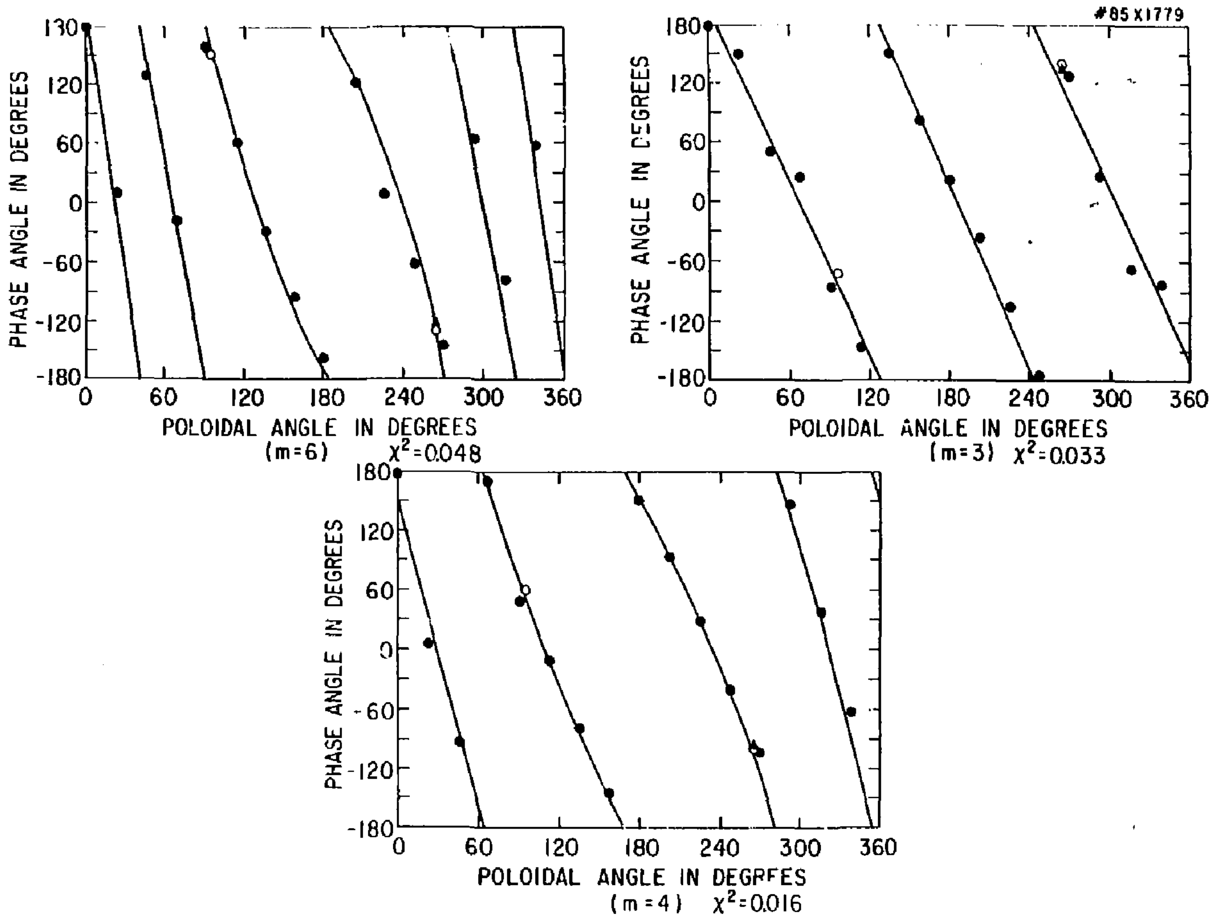
#85 X1779
PHASE ANGLE IN DEGREES
130
120
60
0
-60
-120
-180
0
60
120
180
240
300
360
POLOIDAL ANGLE IN DEGREES
(m=6) χ^2=0.048
PHASE ANGLE IN DEGREES
180
120
60
0
-60
-120
-180
0
60
120
180
240
300
360
POLOIDAL ANGLE IN DEGREES
(m=3) χ^2=0.033
PHASE ANGLE IN DEGREES
180
120
60
0
-60
-120
-180
0
60
120
180
240
300
360
POLOIDAL ANGLE IN DEGREES
(m=4) χ^2=0.016

Fig. 11

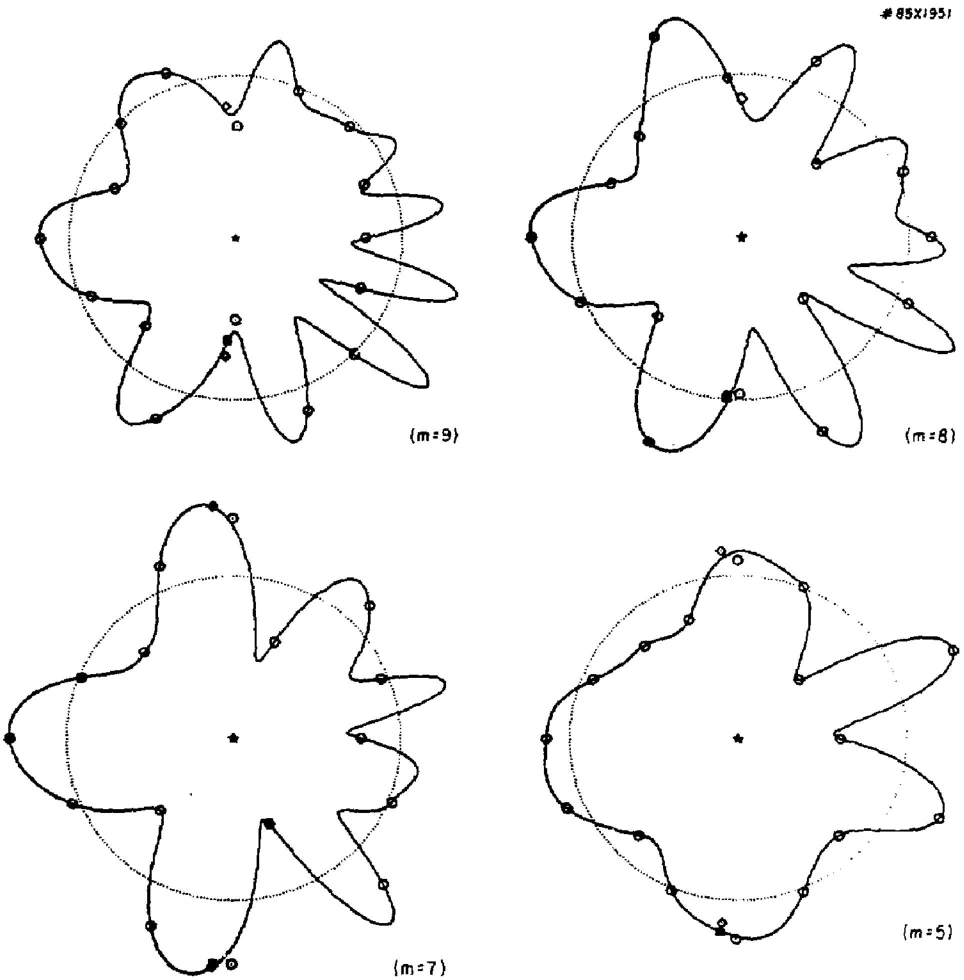

Fig. 12

#85X1781

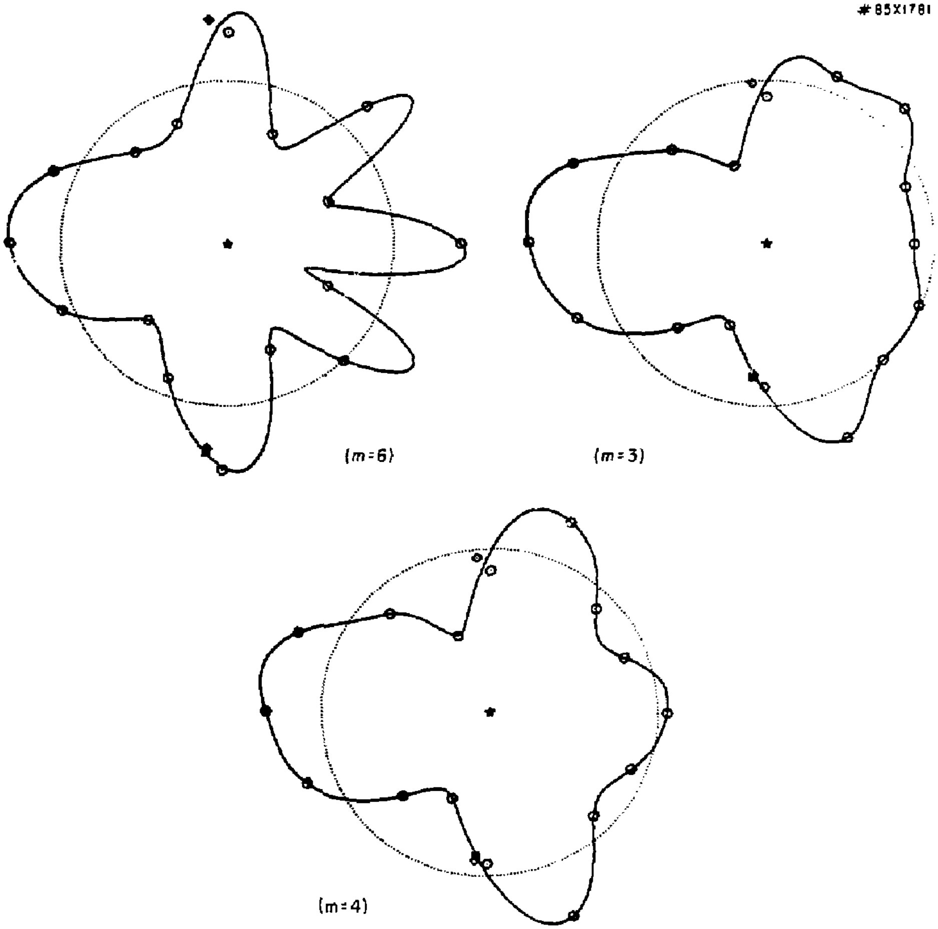
(m=6)
(m=3)
(m=4)

Fig. 13

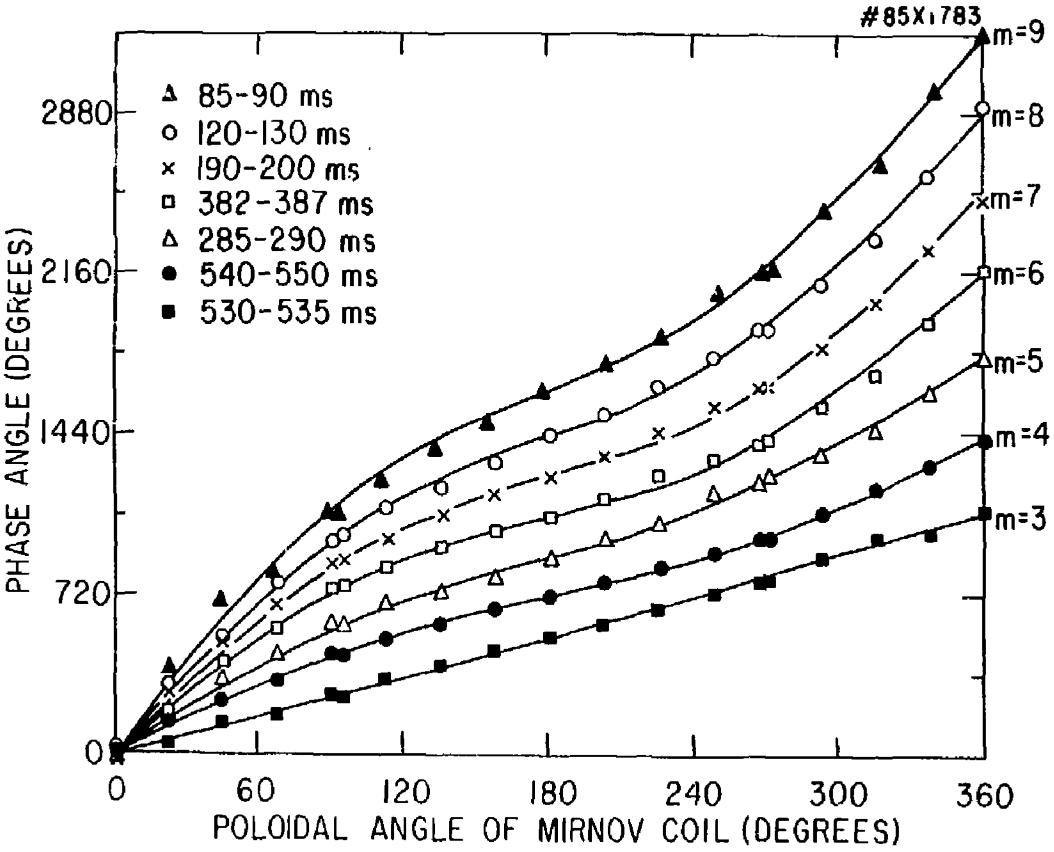
#85X1783
▲ 85-90 ms
○ 120-130 ms
× 190-200 ms
□ 382-387 ms
△ 285-290 ms
● 540-550 ms
■ 530-535 ms
m=9
m=8
m=7
m=6
m=5
m=4
m=3
PHASE ANGLE (DEGREES)
0
720
1440
2160
2880
POLOIDAL ANGLE OF MIRNOV COIL (DEGREES)
0
60
120
180
240
300
360

Fig. 14

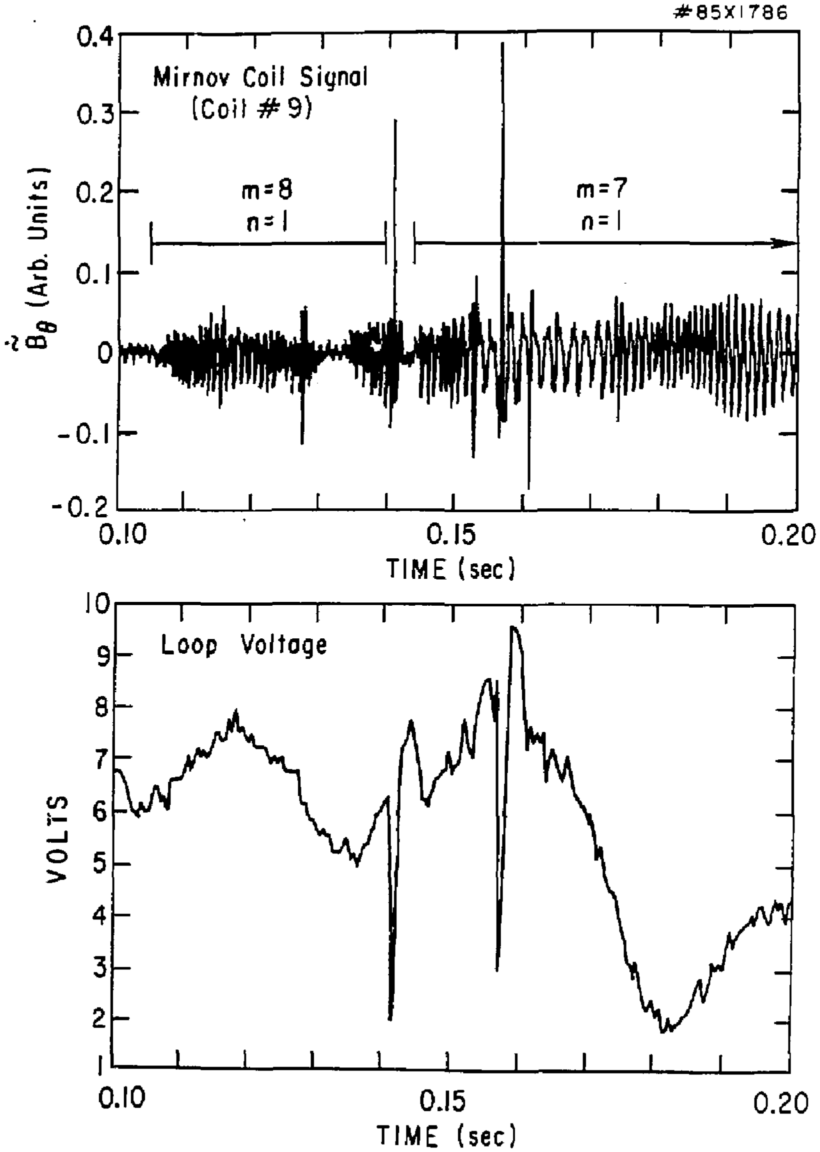
#85X1786
Mirnov Coil Signal
(Coil #9)
m=8
n=1
m=7
n=1
$\tilde{B}_\theta$ (Arb. Units)
0.4
0.3
0.2
0.1
0
-0.1
-0.2
0.10
0.15
0.20
TIME (sec)
Loop Voltage
VOLTS
10
9
8
7
6
5
4
3
2
1
0.10
0.15
0.20
TIME (sec)

Fig. 15

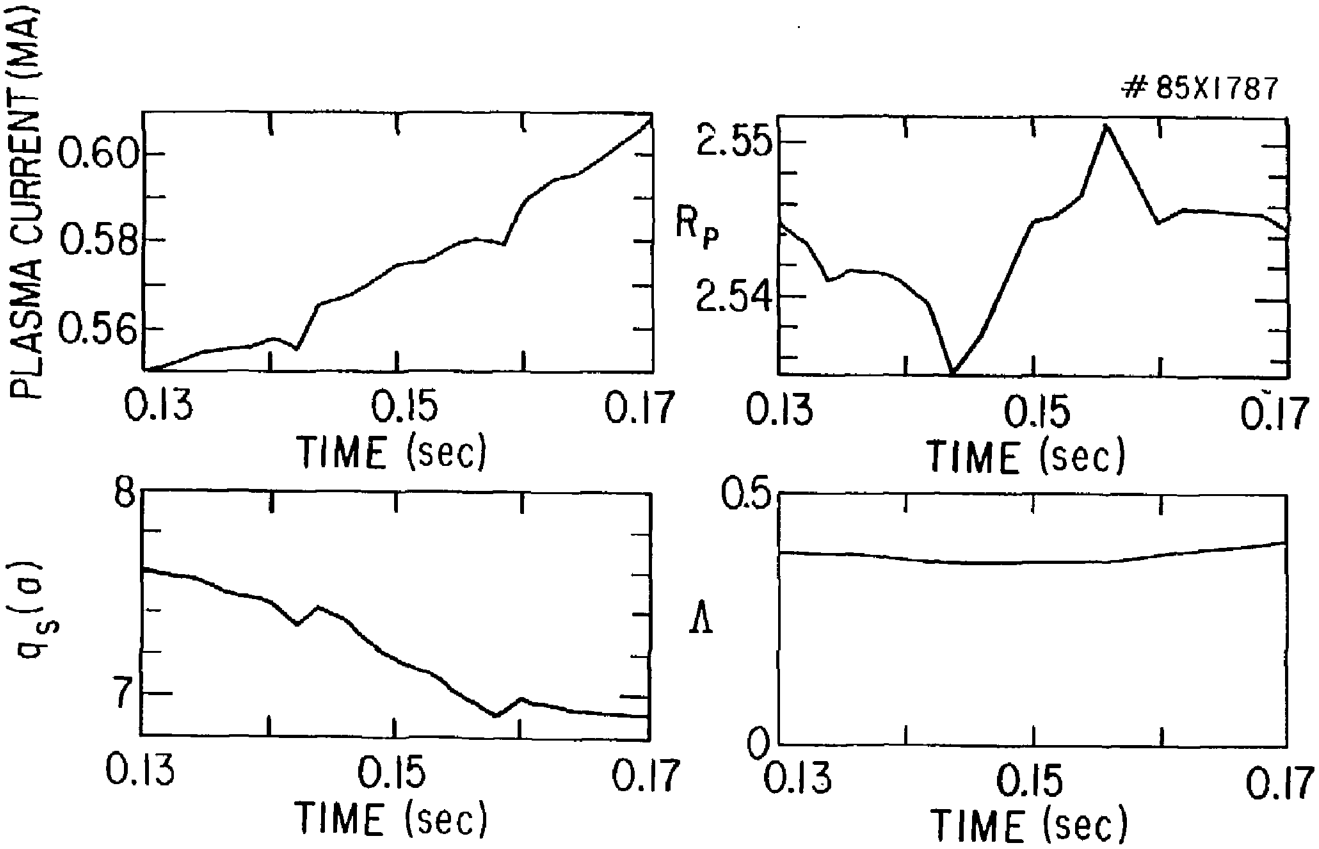
#85X1787
PLASMA CURRENT (MA)
0.60
0.58
0.56
0.13
0.15
0.17
TIME (sec)
R_p
2.55
2.54
0.13
0.15
0.17
TIME (sec)
$q_s(a)$
8
7
0.13
0.15
0.17
TIME (sec)
Λ
0.5
0
0.13
0.15
0.17
TIME (sec)

Fig. 16

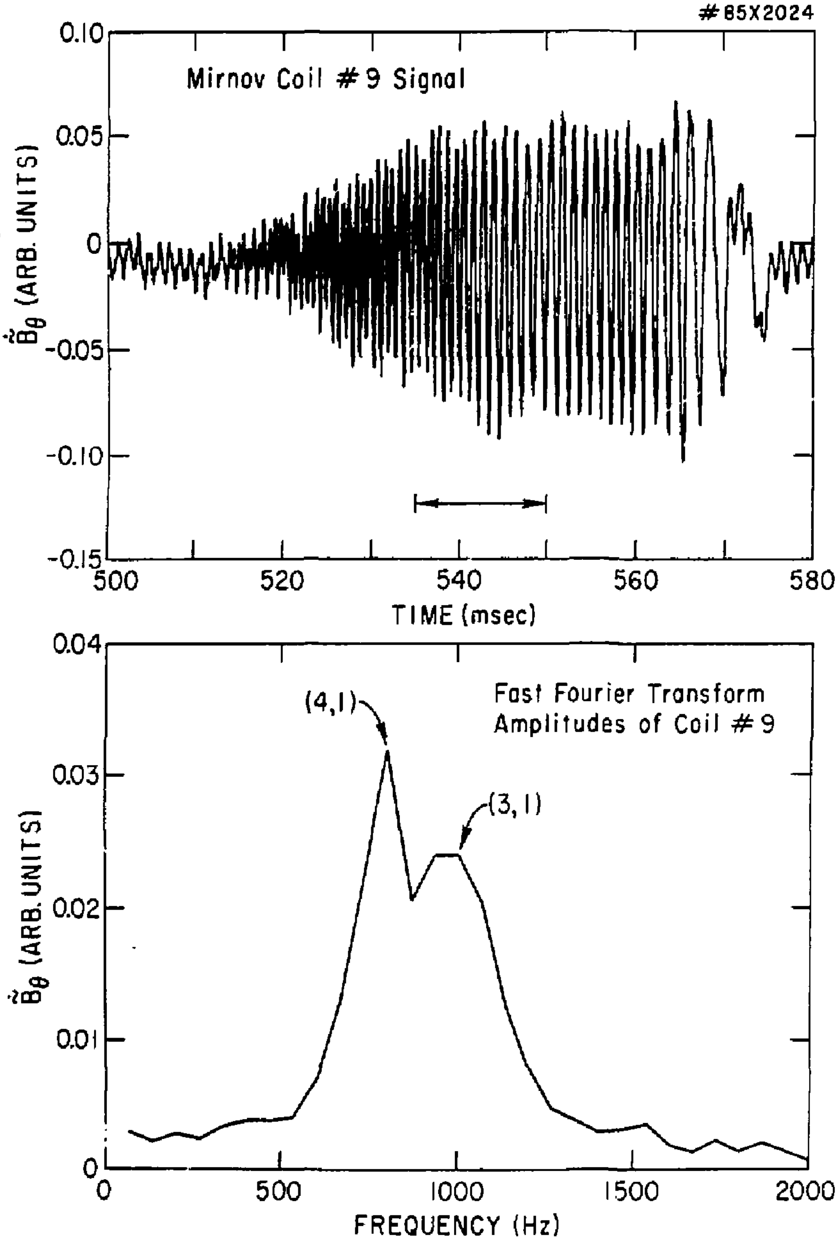

χ^2 (f = 0.8 kHz, m = 4) = 0.010 χ^2 (f = 1.0 kHz, m = 3) = 0.076

Fig. 17

#85X2025

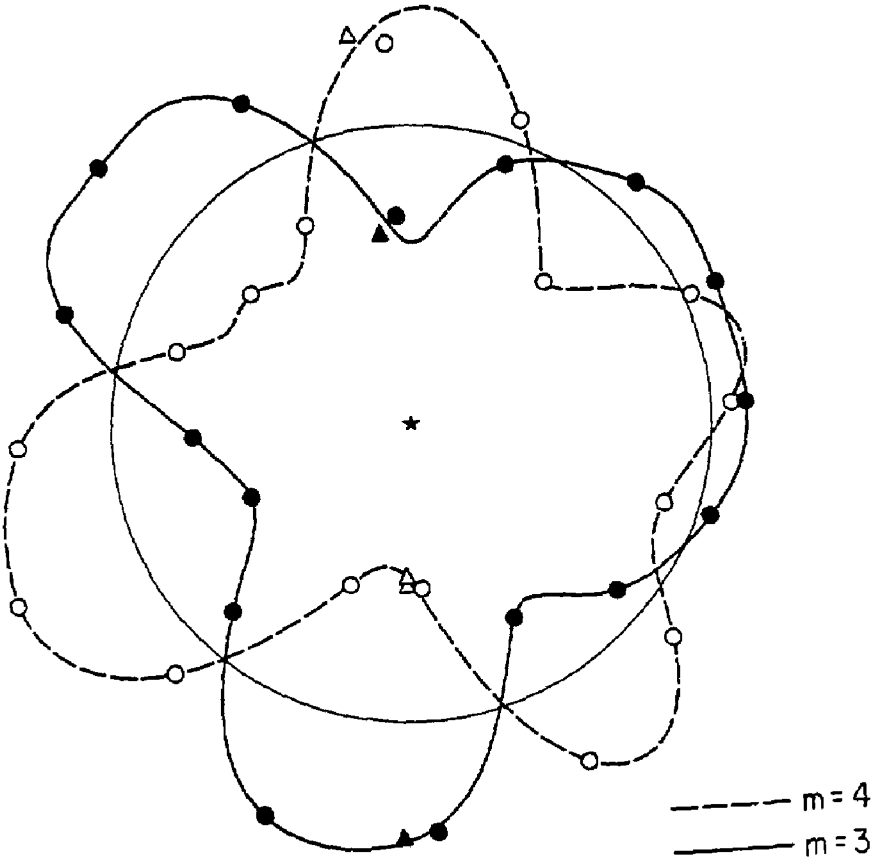

Fig. 18

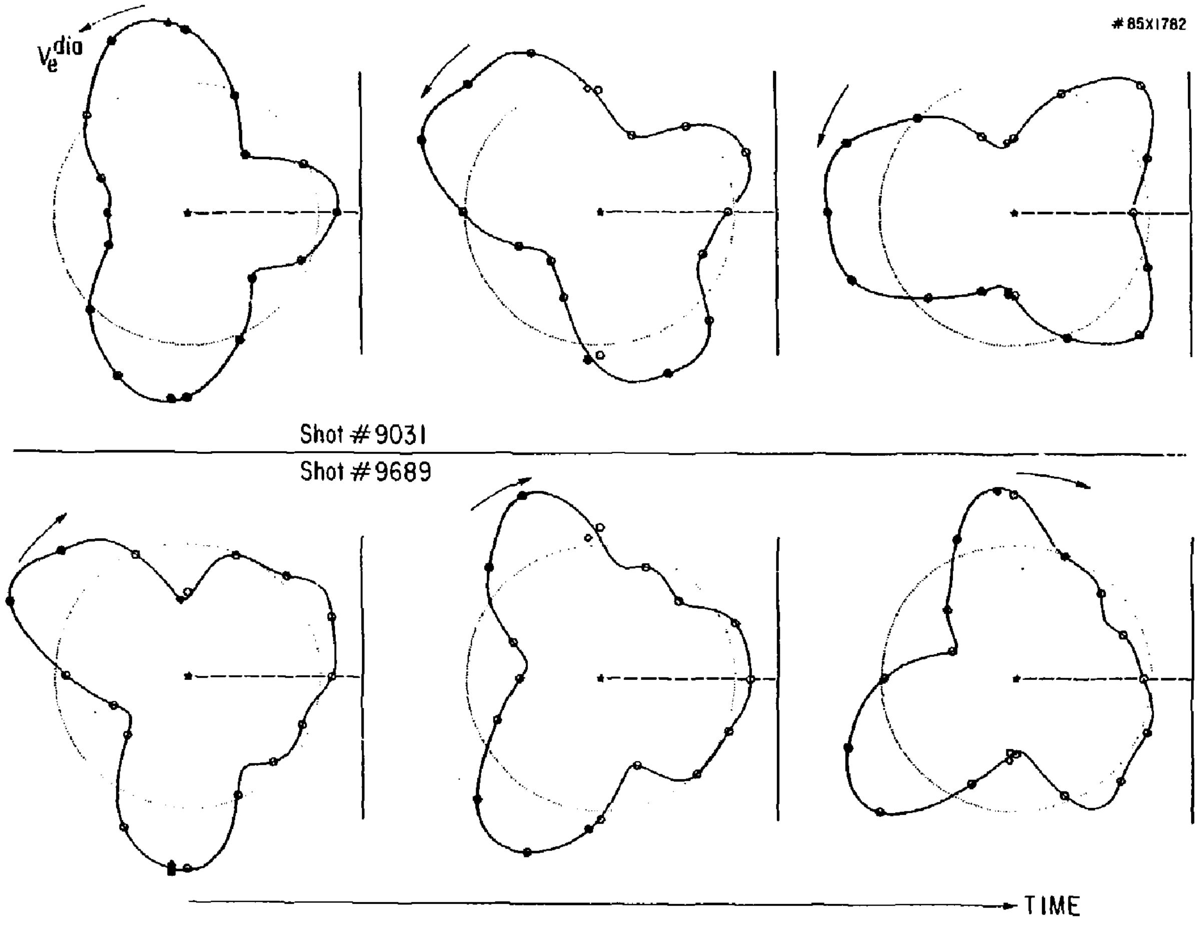

Fig. 19

#85X1784

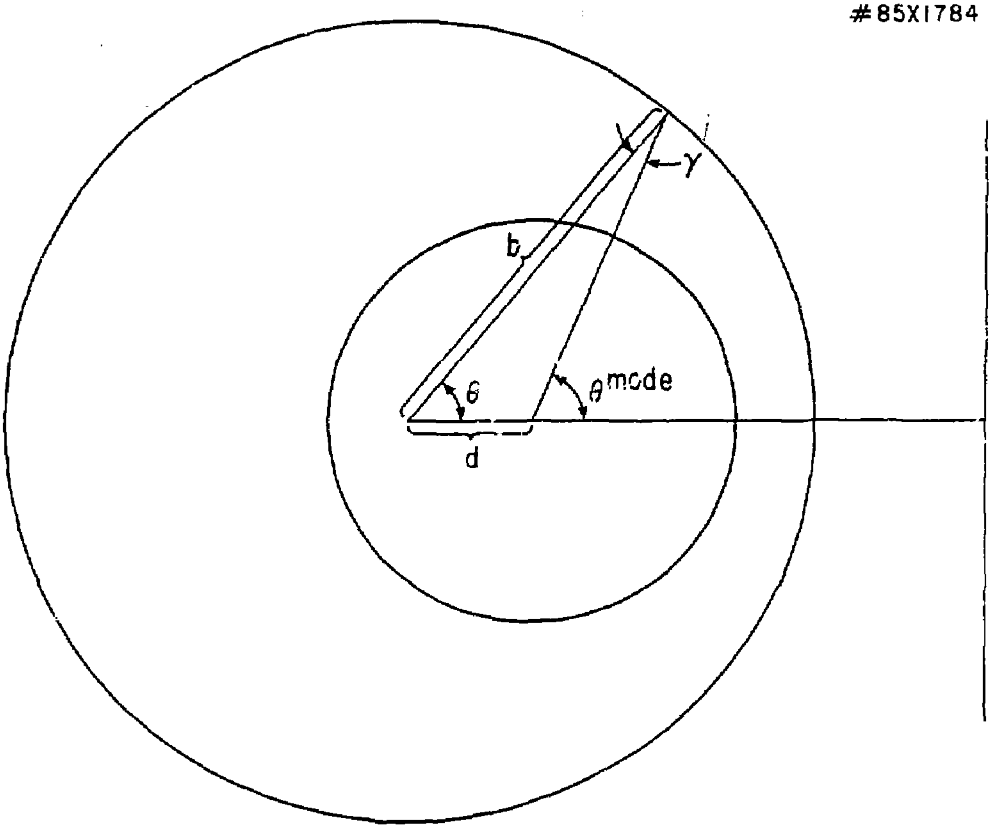

Fig. 20

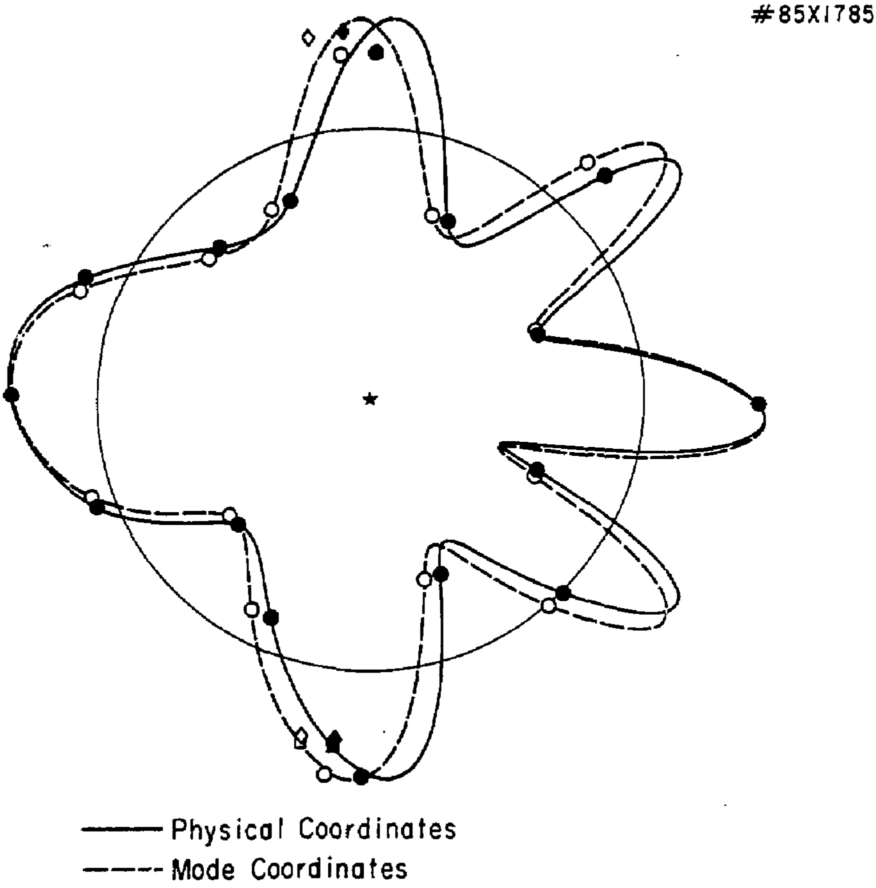

Fig. 21

EXTERNAL DISTRIBUTION IN ADDITION TO UC-20

Plasma Res Lab, Austra Nat'l Univ, AUSTRALIA
Dr. Frank J. Paoloni, Univ of Wollongong, AUSTRALIA
Prof. I.R. Jones, Flinders Univ., AUSTRALIA
Prof. M.H. Brennan, Univ Sydney, AUSTRALIA
Prof. F. Cap, Inst Theo Phys, AUSTRIA
Prof. Frank Verheest, Inst theoretische, BELGIUM
Dr. D. Palumbo, Dg XII Fusion Prog, BELGIUM
Ecole Royale Militaire, Lab de Phys Plasmas, BELGIUM
Dr. P.H. Sakanaka, Univ Estadual, BRAZIL
Dr. C.R. James, Univ of Alberta, CANADA
Prof. J. Teichmann, Univ of Montreal, CANADA
Dr. H.M. Skarsgard, Univ of Saskatchewan, CANADA
Prof. S.R. Sreenivasan, University of Calgary, CANADA
Prof. Tudor W. Johnston, INRS-Energie, CANADA
Dr. Hannes Barnard, Univ British Columbia, CANADA
Dr. M.P. Bachynski, MPB Technologies, Inc., CANADA
Chalk River, Nucl Lab, CANADA
Zhengwu Li, SW Inst Physics, CHINA
Library, Tsing Hua University, CHINA
Librarian, Institute of Physics, CHINA
Inst Plasma Phys, Academia Sinica, CHINA
Dr. Peter Lukac, Komenskeho Univ, CZECHOSLOVAKIA
The Librarian, Culham Laboratory, ENGLAND
Prof. Schatzman, Observatoire de Nice, FRANCE
J. Radet, CEN-BP6, FRANCE
AM Dupas Library, AM Dupas Library, FRANCE
Dr. Tom Mual, Academy Bibliographic, HONG KONG
Preprint Library, Cent Res Inst Phys, HUNGARY
Dr. S.K. Trehan, Panjab University, INDIA
Dr. Indra Mohan Lal Das, Banaras Hindu Univ, INDIA
Dr. L.K. Chavda, South Gujarat Univ, INDIA
Dr. R.K. Chhajlani, Vikram Univ. INDIA
Dr. B. Dasgupta, Saha Inst, INDIA
Dr. P. Kaw, Physical Research Lab, INDIA
Dr. Phillip Rosenau, Israel Inst Tech, ISRAEL
Prof. S. Cuperman, Tel Aviv University, ISRAEL
Prof. G. Rostagni, Univ Di Padova, ITALY
Librarian, Int'l Ctr Theo Phys, ITALY
Miss Clelia De Palo, Assoc EURATOM-ENEA, ITALY
Biblioteca, del CNR EURATOM, ITALY
Dr. H. Yamato, Toshiba Res & Dev, JAPAN
Direc. Dept. Lg. Tokamak Dev. JAERI, JAPAN
Prof. Nobuyuki Inoue, University of Tokyo, JAPAN
Research Info Center, Nagoya University, JAPAN
Prof. Kyoji Nishikawa, Univ of Hiroshima, JAPAN
Prof. Sigeru Mori, JAERI, JAPAN
Library, Kyoto University, JAPAN
Prof. Ichiro Kawakami, Nihon Univ, JAPAN
Prof. Satoshi Itoh, Kyushu University, JAPAN
Dr. D.I. Choi, Adv. Inst Sci & Tech, KOREA
Tech Info Division, KAERI, KOREA
Bibliotheek, Fom-Inst Voor Plasma, NETHERLANDS
Prof. B.S. Liley, University of Waikato, NEW ZEALAND
Prof. J.A.C. Cabral, Inst Superior Tech, PORTUGAL
Dr. Octavian Petrus, ALI CUZA University, ROMANIA
Prof. M.A. Hellberg, University of Natal, SO AFRICA
Dr. Johan de Villiers, Plasma Physics, Nucor, SO AFRICA
Fusion Div. Library, JEN, SPAIN
Prof. Hans Wilhelmson, Chalmers Univ Tech, SWEDEN
Dr. Lennart Stenflo, University of UMEA, SWEDEN
Library, Royal Inst Tech, SWEDEN
Centre de Recherchesen, Ecole Polytech Fed, SWITZERLAND
Dr. V.T. Tolok, Kharkov Phys Tech Ins, USSR
Dr. D.D. Ryutov, Siberian Acad Sci, USSR
Dr. G.A. Eliseev, Kurchatov Institute, USSR
Dr. V.A. Glukhikh, Inst Electro-Physical, USSR
Institute Gen. Physics, USSR
Prof. T.J.M. Boyd, Univ College N Wales, WALES
Dr. K. Schindler, Ruhr Universitat, W. GERMANY
Nuclear Res Estab, Julich Ltd, W. GERMANY
Librarian, Max-Planck Institut, W. GERMANY
Bibliothek, Inst Plasmaforschung, W. GERMANY
Prof. R.K. Janev, Inst Phys, YUGOSLAVIA